Numerical study of dense particle flows under planar shear

Dong, Junhao

2020

Numerical study of dense particle flows under planar shear

JUNHAO DONG | DIVISION OF THEORETICAL CHEMISTRY | LUND UNIVERSITY

Numerical study of dense particle flows under planar shear

by Junhao Dong

LUND
UNIVERSITY

Author(s)
Junhao Dong

Title and subtitle
Numerical study of dense particle flows under planar shear

Abstract

In this thesis I conducted numerical simulations to study the flow behavior of dense particle flows composed of hard particles under planar shear using the discrete element method. The simulations were carried out in two dimensional systems, where the particles are modelled as circular discs. The discs are non-Brownian and neutrally buoyant. The granular flows can be either dry or immersed in a Newtonian fluid, where the fluid is treated in a mean field manner and represented by a velocity profile. The works that are included in this thesis can be divided into two parts.

The first (Paper I +II) focus on the rheology of discontinuous shear thickening (DST) granular flows under *steady* planar shear (*i.e.* with a constant shear-rate $\dot{\gamma}$). The DST behavior is reproduced using the critical load model (CLM), where a threshold force is introduced for determining whether there is friction between the discs at contact. A contact is frictional if the normal force between the discs is larger than the threshold. It is found that a key parameter that controls the rheology of such flow is the fraction of frictional contacts χ_f, defined as the ratio of the number of frictional contacts to the total number of contacts. By performing simulations under controlled imposed pressure, we are able to investigate behaviors of suspensions close to shear jamming points as well as suspensions with intermediate χ_f. The constitutive laws are then presented, which are used to predict rheology of discontinuous shear thickening particle flows under various shear protocols. The types of particle flows range from viscous suspensions where the particles are strictly overdamped so that the particle inertia are negligible to dry granular flows where the particle inertia are dominant, as well as suspensions where both particle inertia and viscous drag is important.

The second part (Paper III and IV) focuses on the behaviors of dense viscous suspensions under *oscillatory* planar shear. The simulations were conducted both with constant packing fraction and constant imposed pressure. The oscillatory shear is either a pure oscillation (*i.e.* $\dot{\gamma}(t) = \gamma_0 \cos(\omega t)$) or with an extra oscillatory shear parallel to a primary shear (*i.e.* $\dot{\gamma}(t) = \dot{\gamma}_0 + \dot{\gamma}_1 \cos(\omega t)$). It is found that by having an oscillatory shear parallel to the primary shear, the viscosity of the suspensions decreased. Furthermore, the shear jamming packing fractions for the suspensions composed of frictional particles are found to be increased under oscillation conditions, possibly due to the microstructure of the suspensions.

Key words: dense suspension, granular flow, shear thickening, oscillatory flow, rheology, discrete element method

Classification system and/or index terms (if any)

I, the undersigned, being the copyright owner of the abstract of the above-mentioned dissertation, hereby grant to all reference sources the permission to publish and disseminate the abstract of the above-mentioned dissertation.

Signature _____

Date ___2020-09-14_____

DOKUMENTDATABLAD enl SIS 61 41 21

Numerical study of dense particle flows under planar shear

by Junhao Dong

LUND
UNIVERSITY

Media-Tryck is an environmentally
certified and ISO 14001:2015 certified
provider of printed material.
Read more about our environmental
work at www.mediatryck.lu.se

MADE IN SWEDEN

Everything flows!
- Heraclitus

Abstract

In this thesis I conducted numerical simulations to study the flow behavior of dense particle flows composed of hard particles under planar shear using the discrete element method. The simulations were carried out in two dimensional systems, where the particles are modelled as circular discs. The discs are non-Brownian and neutrally buoyant. The granular flows can be either dry or immersed in a Newtonian fluid, where the fluid is treated in a mean field manner and represented by a velocity profile. The works that are included in this thesis can be divided into two parts.

The first (Paper I +II) focus on the rheology of discontinuous shear thickening (DST) granular flows under *steady* planar shear (*i.e.* with a constant shear-rate $\dot{\gamma}$). The DST behavior is reproduced using the critical load model (CLM), where a threshold force is introduced for determining whether there is friction between the discs at contact. A contact is frictional if the normal force between the discs is larger than the threshold. It is found that a key parameter that controls the rheology of such flow is the fraction of frictional contacts χ_f, defined as the ratio of the number of frictional contacts to the total number of contacts. By performing simulations under controlled imposed pressure, we are able to investigate behaviors of suspensions close to shear jamming points as well as suspensions with intermediate χ_f. The constitutive laws are then presented, which are used to predict rheology of discontinuous shear thickening particle flows under various shear protocols. The types of particle flows range from viscous suspensions where the particles are strictly overdamped so that the particle inertia are negligible to dry granular flows where the particle inertia are dominant, as well as suspensions where both particle inertia and viscous drag is important.

The second part (Paper III and IV) focuses on the behaviors of dense viscous suspensions under *oscillatory* planar shear. The simulations were conducted both with constant packing fraction and constant imposed pressure. The oscillatory shear is either a pure oscillation (*i.e.* $\dot{\gamma}(t) = \gamma_0 \cos(\omega t)$) or with an extra oscillatory shear parallel to a primary shear (*i.e.* $\dot{\gamma}(t) = \dot{\gamma}_0 + \dot{\gamma}_1 \cos(\omega t)$). It is found that by having an oscillatory shear parallel to the primary shear, the viscosity of the suspensions decreased. Furthermore, the shear jamming packing fractions for the suspensions composed of frictional particles are found to be increased under oscillation conditions, possibly due to the microstructure of the suspensions.

Contents

List of publications

This thesis is based on the following publications, referred to by their Roman numerals:

I   **Analog of discontinuous shear thickening flows under confining pressure**

   J. Dong, M. Trulsson
   Physical Review Fluids, 2(8):081301(R),2017

II   **Unifying viscous and inertial regimes of discontinuous shear thickening suspensions**

   J. Dong, M. Trulsson
   Journal of Rheology, 64(2):255–266,2020

III   **Transition from steady shear to oscillatory shear rheology of dense suspensions**

   J. Dong, M. Trulsson
   submitted to *Physical Review E*

IV   **Oscillatory shear flows of dense suspensions at imposed pressure**

   J. Dong, M. Trulsson
   manuscript

All papers are reproduced with permission of their respective publishers.

Acknowledgements

Popular scientific summary in English

In this thesis, I study the rheology of dense particle flows. The term "rheology" refers to the study of the flow of materials. For example, when we say that blood is thicker than water we are actually talking about that blood has a higher viscosity than water. Viscosity is one of the most commonly characterised properties in rheology. It measures the resistance of a fluid in response to a deformation at a certain rate. The term "particle flow" can be interpreted as flow of granular materials. A granular material is a bunch of solid particles which are usually macroscopic in size. Although the name "granular materials" might not sound familiar, examples of granular materials are found everywhere in daily life.
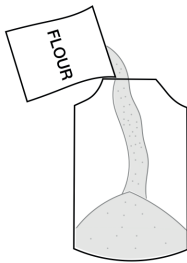
Flour is actually a granular material. When pouring flour into a jar, a granular flow is created. During this process, the flour forms a cone shape in the jar. This is because the interactions between flour grains (*e.g.* friction, cohesion) manage to balance the gravity force. The largest internal angle between the cone surface and the horizontal plane is commonly measured to characterise a granular material, reflecting the surface properties of the grains. After the jar is filled up, one can calculate packing fraction to measure how dense the flour is in the jar, which is defined as the ratio between the volume of the flour and the total volume of the jar. Usually, if you tap the jar there will be more space created on the top. In other words, the flour becomes compacted (*i.e.* reached a higher packing fraction). This is in fact a commonly used technique in engineering to generate granular materials with higher packing fractions.

While the above example given above is a dry granular material (*i.e* the material consist of only particles and no fluid), granular materials can also refer to systems where the particles are immersed in a fluid. Granular materials can display a wide range of behaviors.

If you are a fan of adventure fictions, you are perhaps familiar with the term "quick-sand": those deadly traps that appear in the wild, awaiting careless travellers stepping on them by accident causing the travellers to sink and drown. Quick-sand is a typical example of a shear thinning granular material, although in reality it is usually not that dangerous since a person will not sink entirely. As indicated by the name, the viscosity of a shear thinning material decreases in response to external deformation or stress. In the case of quick-sand, the stress comes from the person who steps on it. The viscosity of the quick-sand decreases causing the person to sink faster.
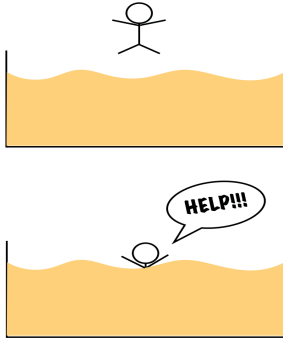
Oobleck (suspensions of corn starch in water with a high packing fraction of the starch) is an example which displays an opposite behavior compared to quick-sand, *i.e.* the viscosity of the material increases when it is subjected to external deformations/stresses. This is usually illustrated by the experiment where you see a person run or jump on a pool of Oobleck without sinking; however the person sinks if he/she stands still. This is because the material thickens when the person runs or jumps, enabling it to support the weight of the person.

With the large variety of the granular materials and their properties, the mechanisms of these properties as well as how to control them remains unclear. My work aims to promote understanding of the behaviors of granular materials and find possible ways to predict or control them. I study how the granular materials behave under planar shear *i.e.* when granular materials are confined between two walls and deformations are applied by moving the planes. The studies are done using computer simulations. To simplify the problem, I assume that all the particles are discs (two dimensional spheres) and that they do not deform. I further assume that the gravity force acting on the particles can be ignored. I focus on the key factors that affect the shear thickening behaviors of the granular flows and propose equations to predict how these flows will behave at various conditions. Another focus of my work is trying to explain why the viscosities of the granular flows decrease when oscillations are applied.

Populärvetenskaplig sammanfattning på svenska

Min avhandling fokusera på reologi av granulära material. Reologi är vetenskapen om materialflödesegenskap. Till exempel, när man säger att blod är tjockare än vatten så menar man egentligen att blod har ett högre viskositet än vatten. Viskositet beskriver hur pass bra ett material kan flöda. Ett granulärt material är (i stora drag) en samling av fasta partiklar vanligtvis större än en mikrometer (ungefär som tjockleken på ett hårstråeller diametern på en röd blodkropp). Vanligtvis så studeras dessa granulära material som de är, dvs. i torrt tillstånd, eller så blandar man dem i en vätska. Det senare kallas för en suspension.

Du kanske känner inte till namnet "granulärt material", men faktum är att granulära material är väldigt vanliga i det daglig livet. Tänk t.ex. på när du häller mjöl i en burk. Det är ett flöde av ett granulärt material. Granulära material visar olika fysikaliska egenskaper. Kvicksand, som oftast beskrivs som en dödlig fara i äventyrsfilmer och böcker, är ett typexemple på ett skjuvtunnande (en reologisk egenskap) material. Materialet, vars viskositet minskar på grund av deformationener eller spänningar. I detta fallet kommer spänningen (dvs. trycket) från människan som trampar på kvicksanden. Kvicksandens viskositet minska och en människa sjunker snabbt ned i kvicksanden..

Oobleck som består av vatten och majsstärkelse är ett annat exempel på ett granulärt material och som beter sig i mostats till kvicksand så ökar oobleck sin viskositet på grund av deformationer eller spänningar. T.ex. kan en människa springa eller hoppa på oobleck utan att hen hinner sjunka ned. Om du står stilla så sjunker du däremot ned i ooblecken.

Mekanismerna som styr de olika egenskaperna hos granulära material är dock forfarande inte helt klarlagda. Min forskning syftar till för en bättre förståelse för granulära materialens beteende och dess underliggande mekanismer. Med hjälp av datorsimuleringar så har jag bland annat studerat skjuvtjockande suspensioner (som t.ex. oobleck) under stadig skjuvning och hur suspensioners reologin skiljer sig mellan stadig skuvning och oscillerande.

Granular materials are piles of discrete particles, where the particle size is typically larger than $100 \mu m$ and are in general polydisperse in both size and shape. The particles can either be dry or immersed in a fluid, with the latter case being called suspensions. Granular materials are widely seen in various industries and natural processes, from daily products such as paint and tooth paste to construction materials such as cement and concrete or geological processes such as land-sliding[1–3]; even the asteroid belt can be viewed as a granular material[4]. Understanding the behaviour of granular materials is therefore of great importance for designing new materials, prohibiting geologic hazard, etc.

At first glance, a granular material might seem to be a simple system. After all, the motion of a single particle is well described by Newton's second law. As for the forces between two particles or between a particle and fluid in the case of suspensions, there are various theories at hand for describing them. For example, Hertz law[5] and Coulomb friction[6] are popular ways of describing the forces between two repulsive particles at contact for normal forces and tangential forces respectively, as they are simple yet able to reproduce most of the physics. In cases of particles in a fluid, forces exerted on the particles from the fluid are also well studied and many equations have been proposed for different conditions[7, 8], for example *Stokes drag*[9] is one of the widely used equations which nicely reproduces the behaviors of spherical particles in laminar flows. Yet granular materials display a wide range of unique behaviours. For example, the pressure at the bottom of a pile of sand saturates quickly and does not further increase as the height of the pile gets larger known as Janssen's effect[10], while pressure for a normal fluid will increase indefinitely with height. Another example is that a pile

of sand requires a critical incline angle to start flowing which is valid also for granular materials composed of frictionless particles while an ordinary flow does not require such a critical angle. In addition, granular materials also dilate at flow. The behavior of granular flows also varies with concentration, in the dilute regime the granular flows can be seen as a dissipative analogue of classic gas; in the dense regime granular flows are shear-rate dependent and have complex rheology[1, 2, 11]. Most of these properties are not well understood and require further investigation.

Several difficulties hinder an accurate description of granular materials. Particles in granular materials are usually macroscopic in size and thermal fluctuations are therefore negligible. The lack of thermal fluctuations inhibits granular materials to explore phase space which can otherwise be well described by statistical thermodynamics. Another difficulty is that the interactions between particles in granular materials are highly dissipative which also distinguish them from the systems described through classic statistical physics. In addition, granular materials lack a clear scale separation between the scales of single granular particle and the whole granular materials which makes the continuum description of granular materials non-trivial[1, 2].

Different techniques have been employed to study granular materials. Photoelastic particles are used to visualise force distribution in granular materials[12]. Various tomography techniques such as electrical tomography[13] and X-ray tomography[14] are used to measure packing fractions of granular materials. Rheology of granular flows can be studied using rheometers with different set-ups such as planar shear, Couette cell[15], inclined plane[16], and rotating drum[17]. Apart from these experimental techniques, numerical simulations are also powerful tools to study granular materials and give access to properties such as the number of contacts which are difficult to measure experimentally.

In my research, I study the rheology of dense granular flows subjected to shear both with and without interstitial fluid using discrete element method (DEM) simulations where particles are described discretely and the fluid is treated as a continuum. I specifically focus on two aspects; one is shear thickening behavior where I try to investigate the role of microscopic friction, *i.e.* at particle contact level, and construct constitutive laws for such flows; the other is oscillatory flows where I study the viscosity reduction as well as shift in shear jamming packing fraction that result from oscillations. The particles in the granular flows I study are hard discs (*i.e.* two dimensional spherical particles) which are repulsive (*i.e.* without any cohesion/attraction) and non-Brownian (*i.e.* all thermal fluctuations are neglected). The particles are considered to be neutrally buoyant and the fluid they are immersed in is Newtonian (*i.e* stresses respond linearly to shear-rate). A more detailed description of models and methods we use will be explained in later sections.

1 Granular packing

One of the most important properties of granular packings is packing fractions,

$$\phi = \frac{V_{\text{particle}}}{V_{\text{total}}}, \tag{2.1}$$

where V_{particle} is the volume occupied by the particles and V_{total} the volume occupied by the whole granular material[1]. Depending on how the packing is created, granular packings can remain stable over a wide range of packing fractions, from a loosest fraction to a densest fraction. For monodisperse hard spheres, one of the simplest types of packings, the densest packing corresponds to a crystalline structure (as illustrated in Fig. 2.1) and the packing fraction can be calculated analytically as $\phi = 0.7404\ldots$ in three dimensions and $0.9069\ldots$ in two dimensions[18]. The crystalline structures are highly ordered, and therefore it is usually difficult for granular materials to obtain crystalline structures. In more common situations, the granular materials are randomly packed. For randomly packed granular materials, the maximum packing fraction is below the crystalline packing fraction and usually referred to as random close packing (RCP). In three dimensions $\phi_{\text{RCP}} \simeq 0.64$[19]; in two dimensions various values of ϕ_{RCP} between 0.82 and 0.89 have been reported[20, 21]. In the opposite limit, the loosest packing is referred to as random loose packing (RLP) which is the minimum packing fraction where the packings are still able to sustain stresses. In three dimensions $\phi_{\text{RLP}} \simeq 0.55$ and in two dimensions $\phi_{\text{RLP}} \simeq 0.60$[22].
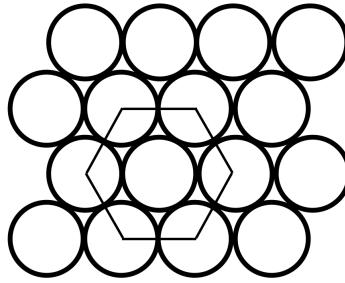
Figure 2.1: A sketch of monodisperse hard spheres in two dimensions showing a hexagonal packing, as indicated by the black lines.

In reality, particles in granular materials are usually of different sizes. An analysis of packings of bidisperse spheres (Fig. 2.2) shows that packings of particles of different sizes can reach a higher ϕ_{RCP} than that for monodisperse packings[1] It should be noted that Fig. 2.2 is an analytical prediction calculated by assuming the size difference between the large and small particles are sufficiently large. The maximum packing fraction becomes smaller if the sizes of the two types of particles get closer to each other. A randomly
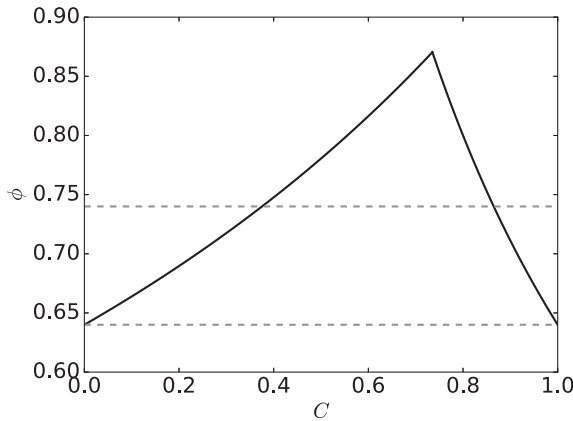
Figure 2.2: Analytical predictions of packing fraction ϕ of packings of bidisperse spheres as function of fraction of large particles C, reproduced from [1]. The grey dashed lines indicate values of crystalline packing fraction $\phi = 0.74$ and random close packing $\phi = 0.64$ for a monodisperse packing.

packed granular material has a packing fraction between ϕ_{RLP} and ϕ_{RCP}. In many industrial applications higher packing fractions are preferred, in order to save space (*e.g.* in transportation of granular materials) or to increase the strength (*e.g.* in cement). There are two main strategies to increase the packing fraction of a randomly packed granular material: through uniaxial compression or through vibration[1]. The former is done by imposing a normal stress on top of granular materials using a piston. As the normal stress increases, particles in the material first undergoes small rearrangements,

then start to deform and eventually break[23]. Vibration is done by attaching a shaker to the material, which allows particles to rearrange without deforming. Vibrations are usually carried out as taps, which allows the material to relax between each period of vibration, to eliminate the influence of the frequency of vibration. Packing fractions increase with the number of taps at the beginning and saturate after certain number of taps. This could be due to that the free space reduces in the process of compaction, which makes it more difficult for the particles to rearrange[1].

1.1   Jamming and number of contacts

A topic that is closely related to close packing is jamming transitions, *i.e.* the transition between jammed and unjammed states. In a jammed state, the packing is able to resist certain stress without having irreversible deformation while in unjammed states the packing is free to flow. Jamming of spherical particles can be divided into three categories[18]; the first is *local jamming* where a particle is locally confined by its neighbors yet they are still able to move together as a cluster (*i.e.* the particles always move with their neighbors); the second is *collective jamming* where particles are not able to displace in groups but may still move in response to external straining (*e.g.* via shearing); the third is *strict jamming* where particles are not allowed to move at all. It should be noted that which jamming category a given packing belongs to is dependent on boundary conditions (*e.g.* hard wall boundary condition or periodic boundary condition), and that in the infinite volume limit collective jamming is the same as strict jamming. While jamming transition can usually be achieved by compaction, it has been shown that jamming can also happen under shear. The shear jamming can be characterised by a strong force network that percolate throughout the packing[24]. The concept of force network will be introduced in the next section.

Now we consider a packing of N frictionless hard particles with diameter d where the total number of contacts in the packing is N_c. The number of degrees of freedom for such a system is ND, where D is the dimension of the system. For hard particles, the distance between coordinates of each pair of particles at contact should equal the particle diameter $|\mathbf{r}_i - \mathbf{r}_j| = d$, where $\mathbf{r}_i$ and $\mathbf{r}_j$ are coordinates of two contacting particles i and j. For N_c contacts we have N_c such equations. To be able to find a solution of the N_c equations (*i.e.* to obtain the coordinates of the particles in the packing), the number of equations needs to be less than the degrees of freedom, which gives $N_c \leq ND$. Otherwise, the system is overdetermined (*i.e.* more equations than unknown variable). A overdetermined system does not have a unique solution. We will refer to $N_c \leq ND$ as a *coordinates argument* later on.

At jamming the packing is isostatic which implies that there is *force balance* for each particle. If the packing is composed of frictionless particles then we only need to con-

sider normal forces, which leads to D equations for each particle and hence ND equations in total. Since there is only one normal force between each pair of contacting particles, the balance of angular momentum is always fulfilled. The unknown variables are the normal forces between all pairs of particles at contact, which equals N_c. In order to find the solutions for the unknown variables, the number of equations should be less than the number of variables, $ND \leq N_c$. At jamming, both the coordinates argument and force balance are fulfilled, leading to $N_c = ND$. Define $Z \equiv 2N_c/N$, which we refer to as the (average) *number of contacts* (or alternatively *coordination number*). At jamming, $Z = 2ND/N = 2D$, which equals 4 in two dimensions and 6 in three dimensions. If the packing is composed of frictional particles we need to consider both force and angular momentum. For each pair of particles at contact, there are two variables, one for the force and one for the torque, which gives $2N_c$ unknown variables in total. Besides D equations for each particles, there is now an extra equation from the torque, resulting in $N(D + 1)$ equations in total. The force balance for the frictional packings then gives $N(D + 1) \leq 2N_c$. To fulfil both coordinates argument and force balance, we obtain $N(D + 1) \leq 2N_c \leq 2ND$ or equivalently $D + 1 \leq Z \leq 2D$ for packings of frictional particles at jamming[1, 25].

1.2   Force distributions

As seen in the previous section, forces play a crucial role in granular packing. However, describing forces in granular materials is not a trivial task due to the large number of contacts, indeterminacy (*i.e.* more unknown variables than equations), etc. Due to the large number of contacts, it is not practical to study every single force between each contact (yet we need to compute each single force in our simulations). The distribution of forces might be of great interest, both experimentally[26] and computationally[27]. Fig. 2.3 illustrates a typical distribution of force magnitudes in granular packings under uniaxial compression where we can see that forces in granular packings are highly heterogeneous. For strong forces, *i.e.* the forces that are larger than the average force $f > \langle f \rangle$, the probability shows an exponential decay with force magnitude, $\mathcal{P}(f) \propto \exp(-\beta f/\langle f \rangle)$, where $\beta \in [1, 2]$ is a constant. For weak forces, the distribution is almost flat and approximately $\mathcal{P}(f) \propto (f/\langle f \rangle)^{\kappa}$ with κ close to zero. It should be noted that Fig. 2.3 is just an approximated illustration and the "measured distribution" might vary with measuring methods. For example, the force distribution measured by the carbon-paper technique displays a peak close to $f = \langle f \rangle$[28]. On the other hand, strong forces ($f > \langle f \rangle$) always have exponential decay regardless of measuring methods. Besides the force magnitude, the direction of forces is also of interest. This is usually characterised by the angular distribution. The angular distribution is used to study both contacts and forces, with the former also referred to as the geometrical fabric and the latter as the mechanical fabric[1]. In two dimensions,
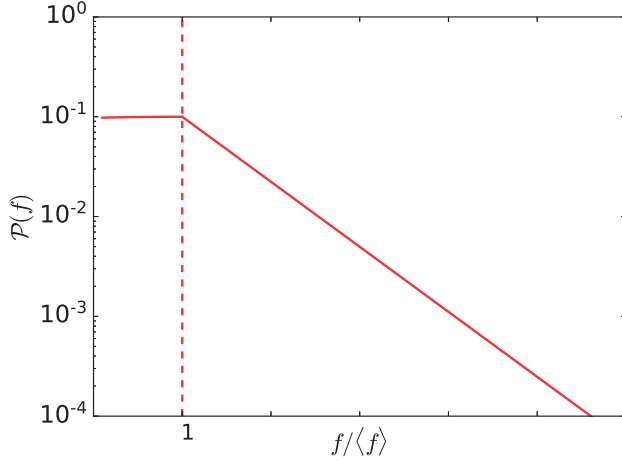
Figure 2.3: A schematic plot illustrating distribution of force magnitude under uniaxial compression; force is normalised by mean force $\langle f \rangle$. The dashed line indicates the place where $f = \langle f \rangle$.

the geometrical fabric is given by a probability density function $\xi(\theta)$ which describes the probability of having contacts at angle θ, where θ is the angle between the vector that connect the centres of two discs at contact and an axis depending on the system (for planar shear, it is the direction of the shear flow), as illustrated in Fig. 2.4(a). In three dimensions, contact between two particles is characterised by two angles θ and ψ so that the probability density function is $\xi(\theta, \psi)$, see Fig. 2.4(b) for illustrations of θ and ψ. Integration of ξ over all angles gives the number of contacts Z. We will now focus on two dimensional situations. Usually, first order Fourier expansion is enough to describe the geometrical fabric[29],

$$\xi(\theta) \approx \frac{1}{2\pi}[1 + A_c \cos 2(\theta - \theta_c)], \qquad (2.2)$$

where A_c gives the amplitude of anisotropy of contact and θ_c is its principal direction. One can alternatively define a fabric tensor[24],

$$\overline{\overline{\mathbf{R}}} = \frac{1}{N'} \sum_{i \neq j} \frac{\mathbf{r}_{ij}}{|\mathbf{r}_{ij}|} \otimes \frac{\mathbf{r}_{ij}}{|\mathbf{r}_{ij}|}, \qquad (2.3)$$

where N' is the number of particles that are in contact, $\mathbf{r}_{ij}$ is contact vector between particle i and j. We denote eigenvalues of $\overline{\overline{\mathbf{R}}}$ as R_1 and R_2. $R_1 + R_2 = Z$ is the number of contacts while $(R_2 - R_1)/Z = A_c/2$ gives the anisotropy[24, 29]. Similarly, the mechanical fabric can also be described by Fourier expansion[29],

$$F_n(\theta) \approx \frac{\langle f \rangle}{2\pi}[1 + A_n \cos 2(\theta - \theta_f)], \qquad (2.4)$$

7
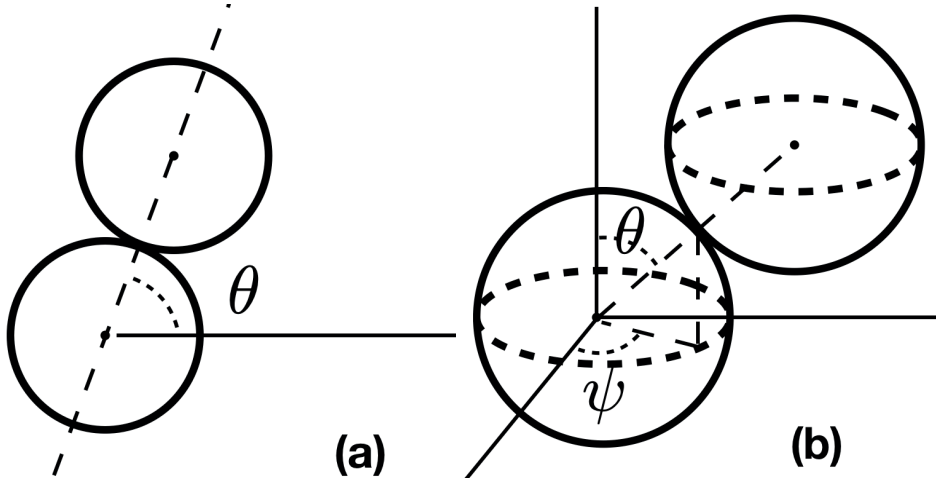
Figure 2.4: Two particles in contact in (a) two dimensions with angle θ, (b) three dimensions characterised by angle θ, ψ.

$$F_t(\theta) \approx \frac{\langle f \rangle}{2\pi} A_t \sin 2(\theta - \theta_f),\tag{2.5}$$

where F_n is the angular distribution of normal forces, F_t the angular distribution of tangential forces, $\langle f \rangle$ the mean force, and A_n and A_t give the magnitude of mechanical anisotropy for normal and tangential force respectively. One can distinguish between strong and weak force networks by plotting the angular distribution function of forces above and below $\langle f \rangle$ separately[1].

2 Granular flow

Granular materials will start to flow when subjected to external stimuli, *e.g.* shaking, planar shearing or inclining. In the dilute regime, particles interact mostly via binary collisions. Granular materials in this regime can be seen as a dissipative analogue of a classic gas and are dominated by kinetic energy. In denser regimes, multi-particle contacts start to play a role and behaviours of granular flows become more closely related to a fluid. Force and contact networks are long-lasting and evolve in flows. Here I will focus on granular flows in the dense regime.

2.1 Planar shear and $\mu(I)$ rheology

Planar shear is one of the most fundamental configurations to study rheology of granular flows. Fig. 2.5 gives a brief illustration of granular flows under planar shear in two dimensions. The axis that is parallel to the velocity gradient is called the extensional

8
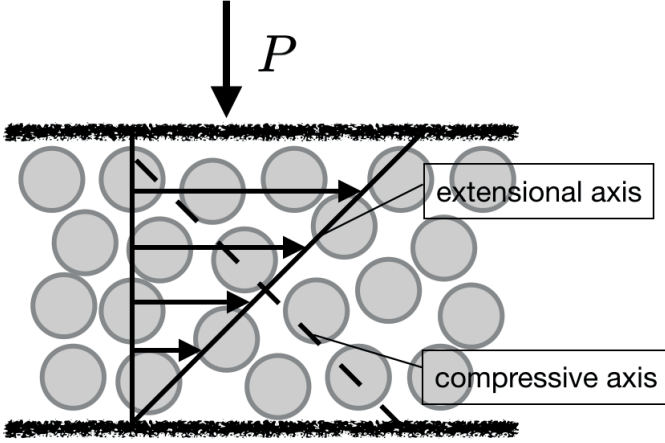
Figure 2.5: A sketch of two dimensional granular materials under planar shear with an imposed pressure P. The arrows indicate velocity profiles in the flow. The extensional and compressive axises are indicated by a solid and a dashed line respectively.

axis while the axis orthogonal is called the compressive axis. The material is confined between two rough walls by an imposed pressure P and are subjected to a constant shear with shear-rate $\dot{\gamma}$. The macroscopic shear-rate is defined as the ratio of the velocity difference between the two walls to the distance between the walls, $\dot{\gamma} = u^w/H$ where u^w is the velocity difference and H is the distance between the walls. Now we consider the case in a large system (*i.e* the distance between two walls is significantly larger than the size of the particles) and that the particles are hard and neutrally buoyant (*i.e.* no gravity) with density ρ_p and diameter d (or average diameter d for polydisperse particles). At steady state, the shear stress σ_{xy} and normal stress σ_n are homogeneous across the system with $\sigma_n = P$. If the imposed pressure P is kept constant, the system is characterised by four parameters: particle diameter d, particle density ρ_p, shear-rate $\dot{\gamma}$ and imposed pressure P. Dimensional analysis suggest that a dimensionless number can be constructed from these four parameters which is referred to as the inertial number[11, 30],

$$I = \frac{|\dot{\gamma}|d}{\sqrt{P/\rho_p}}. \tag{2.6}$$

This parameter can be interpreted as the ratio between a microscopic time scale, $t_{\mathrm{micro}} = d/\sqrt{P/\rho_p}$ *i.e.* the time for a particle to move by d due to imposed pressure P, and a macroscopic time scale, $t_{\mathrm{macro}} = 1/\dot{\gamma}$ *i.e.* the time it takes for a particle to pass another one due to the advected flow[1]. The vertical distance between the two particles is at least d, *i.e.* they do not collide. The packing fraction and the shear stress of the granular material are then functions of I,

$$\sigma_{xy} = \mu(I)P, \tag{2.7}$$

9
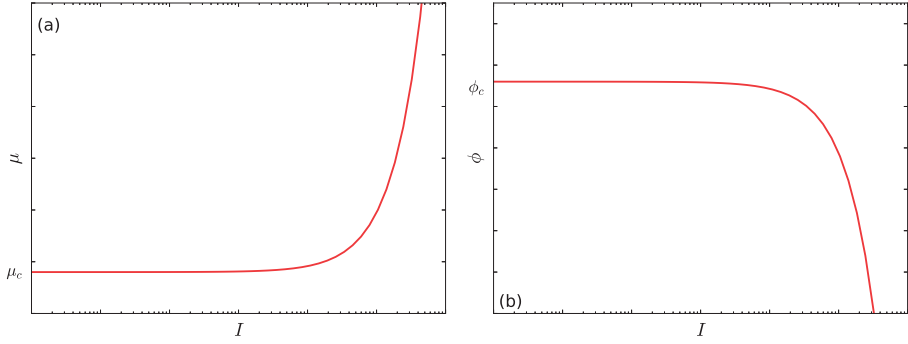
Figure 2.6: Schematic illustrations of (a) $\mu(I)$ and (b) $\phi(I)$ in lin-log scale.

$$\phi = \phi(I), \tag{2.8}$$

where $\mu = \sigma_{xy}/P$ is a macroscopic friction coefficient. Fig. 2.6 show typical shapes of $\mu(I)$ and $\phi(I)$ curves. Both μ and ϕ reach plateaus at vanishing I, as labelled as μ_c and ϕ_c in Fig. 2.6. ϕ_c is the jamming packing fraction and μ_c can be experimentally measured by the avalanching angle (*i.e.* the minimum angle for a granular packing starting to flow).

Using a local rheology assumption, Eq. 2.7 and 2.8 can be generalised to describe inhomogeneous granular flows with $I = |\dot{\gamma}(y)| d / \sqrt{P(y)/\rho_p}$, where $\dot{\gamma}(y)$ and $P(y)$ are the local shear-rate and local pressure, respectively. The equations can further be generalised to tensorial form to describe three dimensional flows sheared in different directions. The components of the total stress tensor Σ_{ij} are written as[31]

$$\Sigma_{ij} = -P\delta_{ij} + \sigma_{ij}, \tag{2.9}$$

where P is the isotropic pressure, $\delta_{ij} = 1$ when $i = j$ and 0 otherwise, and

$$\sigma_{ij} = \eta_{\text{eff}} \dot{\gamma}_{ij}, \tag{2.10}$$

where $\eta_{\text{eff}} = \mu(I)P/|\dot{\gamma}|$ is an effective viscosity, $I = |\dot{\gamma}| d / \sqrt{P/\rho_p}$ and $|\dot{\gamma}| = \sqrt{\dot{\gamma}_{ij}\dot{\gamma}_{ij}/2}$. $\mu(I)$ rheology can be applied to other configurations of granular flows such as flowing on an inclined plane. This formulation has been extensively used both in experimental and computational works[31]. Despite the success of $\mu(I)$ rheology in describing different granular flow behaviours, there are still some limitations. For example, it lacks the links to microscopic properties of granular materials. Furthermore, the quasi-static limit (*e.g.* shear banding) as well as the transition to the dilute regime are not well described[11].

2.2 Bagnold's law

We now consider a granular flow at constant packing fraction ϕ instead of imposed pressure P, *i.e.* the walls in Fig. 2.5 are fixed. The pressure P is now a variable and the system is instead characterised by its packing fraction ϕ, shear-rate $\dot{\gamma}$, particle diameter d and particle density ρ_p. Dimensional analysis suggests that

$$\sigma_{xy} = \rho_p d^2 g_{I,\sigma}(\phi)\dot{\gamma}^2, \tag{2.11}$$

$$P = \rho_p d^2 g_{I,P}(\phi)\dot{\gamma}^2, \tag{2.12}$$

where $g_{I,\sigma}(\phi)$ and $g_{I,P}(\phi)$ are two $\phi-$dependent empirical functions. These two expressions are called Bagnold's law which was first found by Bagnold experimentally when studying sand[32]. Bagnold's law shows that the shear stress σ_{xy} and the pressure P in granular flows have quadratic dependence on the shear-rate $\dot{\gamma}$. Dividing Eq. 2.11 by $\dot{\gamma}$ we obtain,

$$\eta = \rho_p d^2 g_{I,\sigma}(\phi)\dot{\gamma}, \tag{2.13}$$

where $\eta = \sigma_{xy}/\dot{\gamma}$ is the viscosity. At constant ϕ, η scales linearly with shear-rate $\dot{\gamma}$, *i.e.* granular flows are shear thickening.

3 Suspensions: granular materials immersed in a fluid

We have up to now only considered dry granular flows. On the other hand, many applications involves granular particles immersed in a fluid (tooth paste, mud, etc). Such "wet" granular materials are also referred to as suspensions. The fluid introduces a continuum phase, and adds extra contributions to stresses from the fluid, and also affects the equations of motion (due to effects from fluid velocity and extra stress components). The particles we discuss here are still Non-Brownian.

3.1 Navier-Stokes equations

The motion of fluids can be described by the Navier-Stokes equations. The momentum equation can be written as [8],

$$\rho\left[\frac{\partial \mathbf{u}}{\partial t} + (\mathbf{u} \cdot \nabla)\mathbf{u}\right] = \mathbf{f} + \nabla \cdot \overline{\overline{\boldsymbol{\sigma}}}, \tag{2.14}$$

where $\mathbf{u}$ is the fluid velocity, $\mathbf{f}$ is the external body force, $\overline{\overline{\boldsymbol{\sigma}}}$ is the stress tensor

$$\overline{\overline{\boldsymbol{\sigma}}} = \begin{bmatrix} \sigma_{xx} & \sigma_{xy} & \sigma_{xz} \\ \sigma_{yx} & \sigma_{yy} & \sigma_{yz} \\ \sigma_{zx} & \sigma_{zy} & \sigma_{zz} \end{bmatrix}, \tag{2.15}$$

and ρ is the fluid density. The fluid velocity and stress tensor vary in space and time while the fluid density is constant for the models considered here. Under the assumption that fluids are incompressible, in other words that ρ is constant in space and time, the divergence of the fluid velocity vanishes,

$$\nabla \cdot \mathbf{u} = 0. \tag{2.16}$$

The significance of inertial effects from particles compared to viscous drag can be measured by the dimensionless Reynolds number[33, 34],

$$Re = \frac{\rho u L}{\eta_f}, \tag{2.17}$$

where η_f denotes the dynamic viscosity of the fluid and L is a characteristic length scale and $u = |\mathbf{u}|$. If $Re \ll 1$, the inertial terms on left hand side in Eq. 2.14 can be neglected and we get,

$$-\mathbf{f} = \nabla \cdot \overline{\overline{\sigma}}. \tag{2.18}$$

Eq. 2.18 together with Eq. 2.16 are called the Stokes equations. Flows that can be described by Stokes equations are called Stokes flows. From Eq. 2.18, we see that Stokes flows present several unique properties, including linearity (*i.e.* fluid velocity changes linearly with the external force), reversibility (*i.e.* motions are reversible in response to an external force) and instantaneity (*i.e.* motions are not dependent on the history of the system)[8]. A Newtonian fluid is the simplest type of fluid where the shear stress σ_{xy} responds linearly to the shear-rate $\dot{\gamma}$. The stress tensor $\overline{\overline{\sigma}}$ can then be written as [8]

$$\overline{\overline{\sigma}} = -P\overline{\overline{\mathbf{I}}} + \eta_f \overline{\overline{\mathbf{e}}}, \tag{2.19}$$

where P denotes pressure, $\overline{\overline{\mathbf{I}}}$ is the identity tensor and $\overline{\overline{\mathbf{e}}}$ is the strain-rate tensor,

$$\overline{\overline{\mathbf{e}}} = \begin{bmatrix} \frac{\partial u_x}{\partial x} & \frac{1}{2}\left(\frac{\partial u_x}{\partial y} + \frac{\partial u_y}{\partial x}\right) & \frac{1}{2}\left(\frac{\partial u_x}{\partial z} + \frac{\partial u_z}{\partial x}\right) \\ \frac{1}{2}\left(\frac{\partial u_y}{\partial x} + \frac{\partial u_x}{\partial y}\right) & \frac{\partial u_y}{\partial y} & \frac{1}{2}\left(\frac{\partial u_y}{\partial z} + \frac{\partial u_z}{\partial y}\right) \\ \frac{1}{2}\left(\frac{\partial u_z}{\partial x} + \frac{\partial u_x}{\partial z}\right) & \frac{1}{2}\left(\frac{\partial u_z}{\partial y} + \frac{\partial u_y}{\partial z}\right) & \frac{\partial u_z}{\partial z} \end{bmatrix}, \tag{2.20}$$

where u_x, u_y and u_z are the x, y and z component of velocity $\mathbf{u}$. For planar shear, Eq. 2.20 reduces to

$$\overline{\overline{\mathbf{e}}} = \begin{bmatrix} 0 & \dot{\gamma}/2 & 0 \\ \dot{\gamma}/2 & 0 & 0 \\ 0 & 0 & 0 \end{bmatrix}, \tag{2.21}$$

where $\dot{\gamma}$ denotes shear-rate. From Eq. 2.19, the divergence of the stress tensor $\nabla \cdot \overline{\overline{\sigma}}$ can be written as

$$\nabla \cdot \overline{\overline{\sigma}} = -\nabla P + \eta_f \nabla^2 \mathbf{u}. \tag{2.22}$$
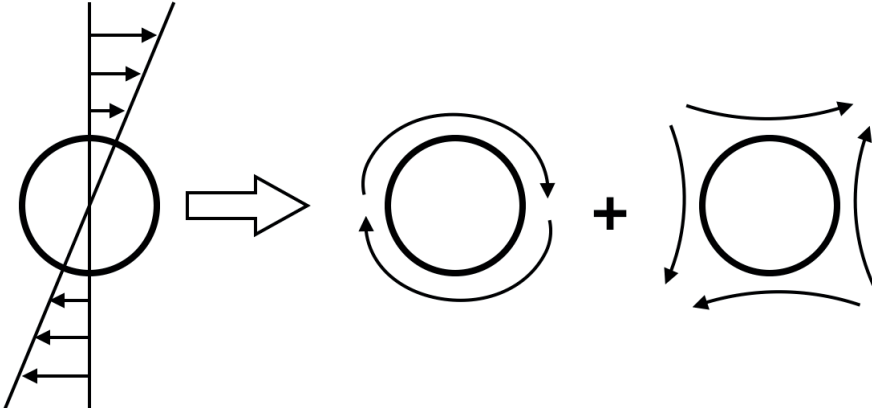
Figure 2.7: Sketch showing decomposition of the motions of a particle in a shear flow into rotation and strain, as indicated by arrows.

Combining Eq. 2.22 with Eq. 2.18 we get

$$-\mathbf{f} = -\nabla P + \eta_f \nabla^2 \mathbf{u}. \tag{2.23}$$

Here we will always consider the fluid to be Newtonian.

3.2 From dilute suspensions to dense suspensions

Now we consider particles in a fluid. We start with an extreme case where one single particle is immersed in a fluid under shear, with shear-rate $\dot{\gamma}$. Motions of such a particle can be decomposed into rotational and strain motion, as illustrated in Fig. 2.7. The velocity of the sheared fluid is [8]

$$\mathbf{u}^\infty = (\overline{\overline{\mathbf{E}}}^\infty + \overline{\overline{\Omega}}^\infty) \cdot \mathbf{x}, \tag{2.24}$$

where the fluid strain-rate tensor $\overline{\overline{\mathbf{E}}}^\infty = \langle \overline{\overline{\mathbf{e}}} \rangle$. The superscript ∞ indicates the velocity far away from the particle (*i.e.* no disturbance from the particle). Assuming a no-slip boundary condition at the fluid-particle interface, the fluid rotational velocity tensor $\overline{\overline{\Omega}}^\infty$ and the particle rotational velocity $\boldsymbol{\omega}^p$ are related by

$$\overline{\overline{\Omega}}^\infty \cdot \mathbf{x} = \boldsymbol{\omega}^p \times \mathbf{x}, \tag{2.25}$$

and the $\overline{\overline{\mathbf{E}}}^\infty$ and the particle velocity $\mathbf{u}^p$ are related by

$$\overline{\overline{\mathbf{E}}}^\infty \cdot \mathbf{x} = \mathbf{u}^p, \tag{2.26}$$

where $\mathbf{x}$ is the position vector. The effect of the particle on the streamlines of the fluid is illustrated in Fig. 2.8. The particle furthermore experiences a hydrodynamic force from
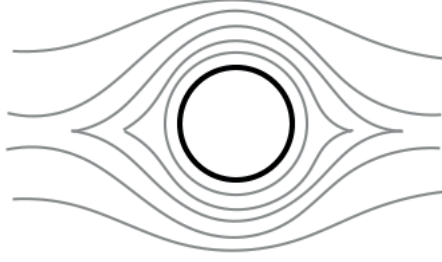
Figure 2.8: Sketch showing streamlines of fluid with presence of the particle, as indicated by grey lines; all streamlines are symmetric and the closed streamline near the particle shows rotational dominating motion.

the fluid. From Eq. 2.23, 2.24 and 2.26, an expression for the hydrodynamic force $\mathbf{F}^h$ can be derived,

$$\mathbf{F}^h = 3\pi\eta_f d(\mathbf{u}^\infty - \mathbf{u}^p), \tag{2.27}$$

where d is the particle diameter, $\mathbf{u}^\infty$ is the fluid velocity. This is also called the viscous drag force or Stokes drag. The fluid also exerts a hydrodynamic torque on the particle, which can be derived in a similar way, from Eq. 2.23, 2.24 and 2.25,

$$\mathbf{T}^h = \pi\eta_f d^3(\boldsymbol{\omega}^\infty - \boldsymbol{\omega}^p), \tag{2.28}$$

where $\boldsymbol{\omega}^\infty$ is the rotational velocity of the fluid.

Now we consider dilute suspensions, where the particles are far apart so that there are no interactions between them. Due to the disturbance introduced by adding particles to the flow field, the viscosity of the suspension η increases with increasing number of solid particles (*i.e.* the solid packing fraction ϕ)[35]. The viscosity η of the suspensions can therefore be written as

$$\eta = \eta_f g_J(\phi), \tag{2.29}$$

where η_f is the viscosity of the fluid and $g_J(\phi)$ is a function dependent on particle packing fraction. To compute $g_J(\phi)$ in the dilute regime, we start from the total stress [8]

$$\overline{\overline{\Sigma}} = -\langle P\rangle\overline{\overline{\mathbf{I}}} + 2\eta_f\langle\overline{\overline{\mathbf{e}}}\rangle + \overline{\overline{\Sigma}}^p, \tag{2.30}$$

where $\langle P\rangle$ is the average pressure and $\overline{\overline{\Sigma}}^p$ is the particle contribution to the stress which in the dilute regime is given by fluid-particle stress since there are no collisions between particles

$$\overline{\overline{\Sigma}}^p = 5\phi\eta_f\langle\overline{\overline{\mathbf{e}}}\rangle. \tag{2.31}$$

The total stress tensor is then

$$\overline{\overline{\Sigma}} = -\langle p\rangle\overline{\overline{\mathbf{I}}} + 2\eta_f\left[1 + \frac{5}{2}\phi\right]\langle\overline{\overline{\mathbf{e}}}\rangle. \tag{2.32}$$

For planar shear, we get an expression for the shear stress σ_{xy},

$$\sigma_{xy} = \eta_f\left[1 + \frac{5}{2}\phi\right]\dot{\gamma}. \tag{2.33}$$

Rearranging Eq. 2.33 using $\eta = \sigma_{xy}/\dot{\gamma}$, we have $g_J(\phi) = 1 + (5/2)\phi$ and $\eta = \eta_f[1 + (5/2)\phi]$, which is the *Einstein viscosity* [36]. As the packing fraction increases, pair interactions between particles are needed, while many-body interactions are still negligible. A higher order term then needs to be included in $g_J(\phi)$ [37, 38],

$$g_J(\phi) = 1 + \frac{5}{2}\phi + 6.95\phi^2, \tag{2.34}$$

which indicates that the viscosity increases more rapidly than the Einstein viscosity as the packing fraction increases.

As the packing fraction increases further, many-body interactions between particles become significant. The shear stress can still be written in the general form of Eq. 2.33 [35]

$$\sigma_{xy} = \eta_f g_{J,\sigma}(\phi)\dot{\gamma}, \tag{2.35}$$

which indicates a linear scaling of the shear stress σ_{xy} with the shear-rate $\dot{\gamma}$, unlike Eq. 2.11 for dry granular flows where the shear stress σ_{xy} scales quadratically with the shear-rate $\dot{\gamma}$. It is generally considered difficult to get an analytical expression of Eq. 2.35 in the dense regime (although a semi-analytical expression for frictionless suspensions has been derived with an empirical parameter included [39]). Instead, empirical functions are introduced to relate viscosity and packing fraction. One such function has the form [35, 40, 41]

$$\eta/\eta_f = g_{J,\sigma}(\phi) \sim (\phi_c - \phi)^{-n}, \tag{2.36}$$

where ϕ_c is the jamming packing fraction which depends on microscopic friction and n is a positive constant. A schematic plot of such a relation is shown in Fig. 2.9. This relation has been shown to nicely describe both experiments[42–44] and simulation results[45–47]. At shear jamming, suspension stresses (and viscosities) are dominated by stresses from particle-particle interactions. One can therefore use the same isostatic argument as in dry granular flows, which gives the number of contacts Z at jamming with $Z = 2D$ for suspensions consisting of frictionless particles and $D + 1 \leq Z \leq 2D$ for suspensions consisting of frictional particles, where D is the dimension of the system. Suspensions consisting of frictionless particles have a larger Z at jamming, leading to a higher jamming packing fraction ϕ_c, as illustrated in Fig. 2.9

3.3   From $\mu(I)$ to $\mu(J)$ rheology

While a study on rheology of dense suspensions is usually carried out under constant packing fraction, there have been set-ups developed for constant imposed pressure P as
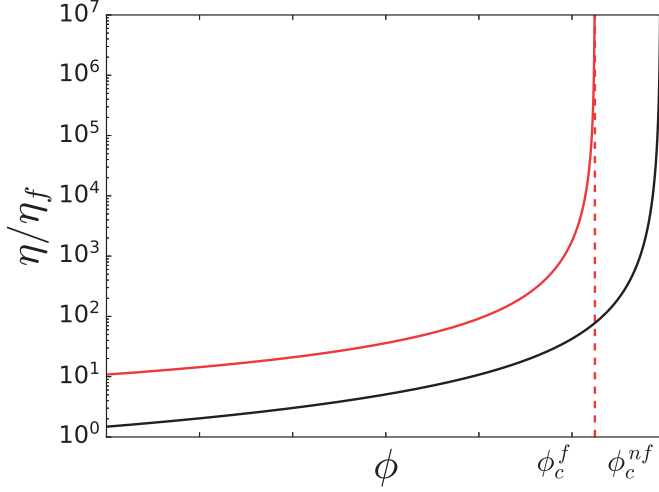
Figure 2.9: Lin-log plots showing the relation between η/η_f and ϕ in the dense regime; the red line corresponds to a frictional suspension while the black line correspond to a frictionless suspension; the dashed line indicates divergence of η/η_f as $\phi \to \phi_c$; ϕ_c^f denotes the jamming packing fraction for a frictional suspension (*i.e.* a suspension composed of frictional particles) and ϕ_c^{nf} denotes the jamming packing fraction for a frictionless suspension.

illustrated in Fig. 2.10. This set-up is similar as in Fig. 2.5 for dry granular flows. The difference is that the walls are now porous and the whole set-up is immersed in a fluid so that the fluid can freely move in and out when the walls move. For such a system, the macroscopic time scale remains the same as in the dry granular flow case, $t_{\mathrm{macro}} = 1/\dot{\gamma}$. The microscopic time scale, on the other hand, can vary depending on the experimental conditions[1, 8]. Here we consider the viscous regime, where the particles are neutrally buoyant (*i.e.* no effect from gravity) and overdamped (*i.e.* negligible particle inertia) and the flows are steady. The microscopic time scale is then dependent on the viscous drag and the imposed pressure which gives $t_{\mathrm{micro}} = \eta_f/P$. We can then form a dimensionless number for suspensions in the viscous regime which is usually referred to as the viscous number (a counterpart of I and sometimes denoted as I_v)[42],

$$J = \frac{t_{\mathrm{micro}}}{t_{\mathrm{macro}}} = \frac{\eta_f \dot{\gamma}}{P}. \tag{2.37}$$

Dimensional analysis implies that the rheology of the suspensions is characterised by the viscous number J according to,

$$\sigma_{xy} = \mu(J)P, \tag{2.38}$$

$$\phi = \phi(J). \tag{2.39}$$

Similarly as Eq. 2.35, one can write the expression for P,

$$P = \eta_f g_{J,P}(\phi)\dot{\gamma}. \tag{2.40}$$
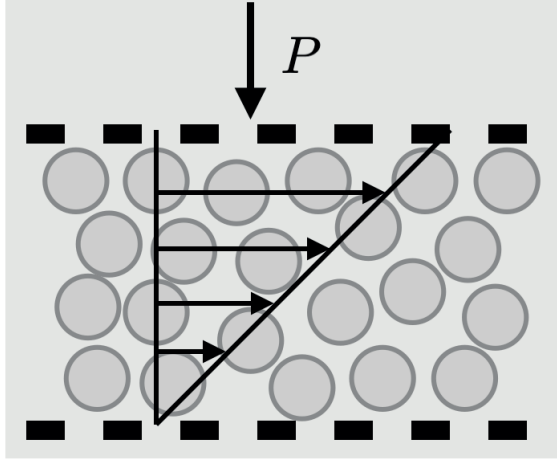
Figure 2.10: A sketch of a two dimensional granular materials immersed in a fluid with an imposed pressure P. The top and bottom walls are porous so that the fluid can freely flows in and out when the walls move. The arrows indicate velocity profiles in the flow.

Eqs. 2.35 and 2.40 show that both shear stress σ_{xy} and pressure P scale linearly with shear-rate $\dot{\gamma}$ in suspensions where viscous drag dominates.

3.4 Combination of $\mu(I)$ and $\mu(J)$ rheology

So far, I have discussed dry granular flows, which are characterised by I, and suspensions in the viscous regime, which are characterised by J. These two cases can be seen as two limits. One is dominated by particle inertia while another is dominated by viscous drag. On the other hand many suspensions are influenced by contributions from both particle inertia and viscous drag. This can be illustrated by *Stokes number*, $St = I^2/J = \rho_p \dot{\gamma} d^2/\eta_f$. Dry granular flows correspond to $St \to \infty$ while suspensions in the viscous regime correspond to $St \to 0$. Suspensions with both particle inertia and viscous drag contributions give finite St. To characterise such suspensions, we first make an assumption that shear stress σ_{xy} and pressure P of such suspensions are linear combinations of contributions from particle inertia and viscous drag[48–50]. Combining Eqs. 2.11 with 2.35 and Eqs. 2.12 with 2.40, we have

$$\sigma_{xy} = \eta_f g_{J,\sigma}(\phi)\dot{\gamma} + \rho_p d^2 g_{I,\sigma}(\phi)\dot{\gamma}^2, \tag{2.41}$$

$$P = \eta_f g_{J,P}(\phi)\dot{\gamma} + \rho_p d^2 g_{I,P}(\phi)\dot{\gamma}^2. \tag{2.42}$$

The divergence of $g_I(\phi)$ is either the same as that of $g_J(\phi)$ or steeper than $g_J(\phi)$, according to different studies [35, 39, 48, 51, 52]. In my work, we make the approximation that $g_J(\phi)$ and $g_I(\phi)$ have the same divergence, so that $g_{I,\sigma}(\phi) = \alpha g_{J,\sigma}(\phi)$ and

$g_{I,\sigma}(\phi) = \alpha g_{J,\sigma}(\phi)$ where α is an empirical constant depending on the system. Rewriting Eqs. 2.41 and 2.42 and dividing by P, we get

$$g_{J,\sigma}(\phi) = \frac{\mu}{J + \alpha I^2}, \tag{2.43}$$

$$g_{J,P}(\phi) = \frac{1}{J + \alpha I^2}. \tag{2.44}$$

From these two equations, one can define a new dimensionless parameter K characterising the suspensions for all values of I and J[48, 51],

$$K = J + \alpha I^2. \tag{2.45}$$

The shear stress and packing fraction are then functions of K

$$\sigma_{xy} = \mu(K)P, \tag{2.46}$$

$$\phi = \phi(K). \tag{2.47}$$

3.5 Shear thickening

Shear thinning and shear thickening are common behaviors observed for dense suspensions. Toothpaste, paint and hand cream are all examples of shear thinning suspensions and corn starch suspensions (also called "oobleck") is the most common example of shear thickening suspensions. As indicated by its name, shear thickening is
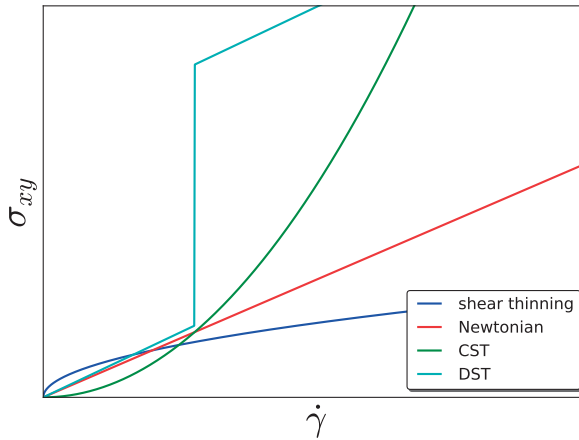
Figure 2.11: A schematic plot showing how shear stress σ_{xy} respond to shear-rate $\dot{\gamma}$ in Newtonian, shear thinning, continuous shear thickening (CST) and discontinuous shear thickening (DST) suspensions.

a non-Newtonian behavior where viscosities of dense suspensions increase with shear-rate. Depending on the magnitude and sharpness of the increase in viscosity, shear thickening is further classified into *continuous shear-thickening* (CST), where viscosity increases continuously, and *discontinuous shear-thickening* (DST), where viscosity increases drastically above a certain threshold in shear-rate [3, 52–54]. Fig. 2.11 illustrate schematically how shear stress σ_{xy} responds to shear-rate $\dot{\gamma}$, if the suspension is shear-thinning, Newtonian, continuous shear-thickening and discontinuous shear-thickening. It has been shown that suspensions which display CST behavior can transit to DST behavior, as the packing fraction increases [45, 55]. Because of its complex physics, and potential industrial applications such as liquid body armour and brake fluid, shear thickening has received much attention. Several mechanisms have been proposed to explain shear thickening for different types of dense suspensions. For example, suspensions of nonionic surfactants display DST because of the tilting of lamellar structures and formation of multilamellar vesicles [56]. Here we focus on suspensions consisting of hard non-Brownian particles. One explanation of shear thickening behavior is hydroclustering[57]. When two particles approach, a short range lubrication force results in an increased hydrodynamic pressure, which causes depletion of fluid between the particles. As shown schematically in Fig. 2.12, the lubrication force increases as the gap between two particles and eventually diverges. Since the fluid between the two particles is Stokesian (*i.e.* flows are time reversible), the force that is required to separate the two particles will be of the same magnitude. Therefore, particles tend to stick
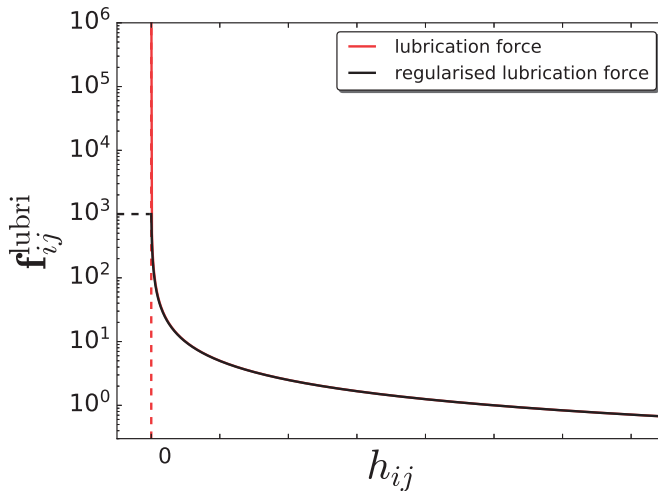
Figure 2.12: A schematic lin-log plot of lubrication force (red solid line) between two particles with minimum separation h_{ij}. The black solid line is a schematic plot of a regularised lubrication force.

together and form larger clusters. These hydroclusters have higher dissipation leading to an increased viscosity. Although this mechanism manages to explain CST behavior,

it lacks a specific time scale for DST (*i.e.* the time given by the threshold shear-rate of the on-set of DST). It is also unable to explain the drastic viscosity increase found in DST.

(a) **(b)**

increasing $\dot{\gamma}$
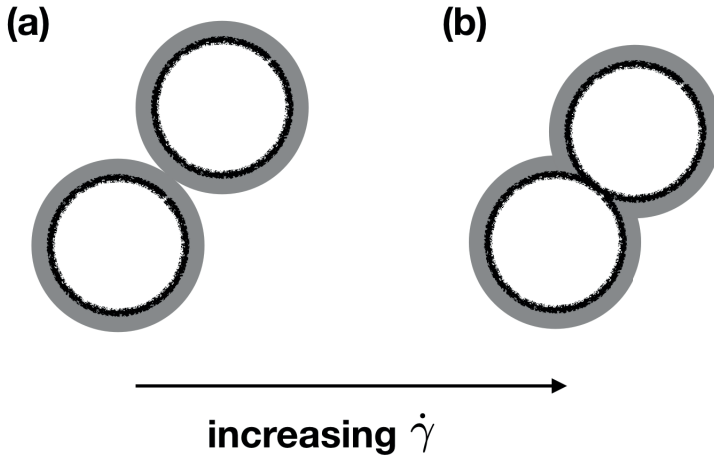
Figure 2.13: Sketch showing two rough particles stabilized by a repulsive layer at (a) low shear-rate and (b) after this barrier is overcome at higher shear-rate; particles are indicated by black circles and repulsive layers by grey rings.

Another mechanism considers friction between particles [58, 59]. The mechanism is schematically illustrated in Fig. 2.13. Particles in suspensions are usually stabilized by repulsive forces, such as electrostatic forces and steric interactions. When two particles approach each other, they first contact via the repulsive layer which is non-frictional. At low shear-rate, particles are not able to get closer. However, as the shear-rate increases, forces acting on particles become large. When the force is larger than the repulsive barrier, the surfaces of the particles are able to touch. And since surfaces are usually rough, such contacts introduce extra tangential forces into the system, leading to an increased viscosity. The shear-rate where most repulsive barriers are overcome is the threshold shear-rate. This mechanism has been verified by recent experiments[17, 60], where negatively charged polystyrene particles are used and the repulsive electrostatic force is controlled by salt concentration. The result shows that DST behavior becomes less significant (*i.e.* the increase in viscosity becomes smaller) as salt concentration increases (*i.e.* the more the electrostatic repulsive forces are screened), indicating a close relation between DST and repulsive interaction. According to this mechanism, unthickened suspensions can be seen as a non-frictional suspensions while suspensions after thickening are viewed as frictional suspensions. Two kinds of suspensions display different rheology. Suspensions under transition can thus be described by mixture of two states, where some particles are in frictional contact and others are in frictionless contact. The rheology of a DST suspension is a combination of the rheology of non-frictional and frictional suspensions weighted by the composition of the two states, as

proposed by the "Wyart-Cates model" [61].

In addition to the frictional contact mechanism, a recent study proposed an alternative friction model[62]. According to this model, the DST behavior is attributed to the lubrication force after taking the surface roughness of the particles into account. The surface roughness is described as asperities on the surfaces. As two particles approach, so that the separation between the particles is of the same magnitude as the size of the asperities, the lubrication force between the asperities becomes non-negligible. As illustrated in Fig. 2.14, the asperities introduces extra separations h'_{ij} (and hence a lubrication force $\propto 1/h'_{ij}$) in addition to the separation between the particles h_{ij}. The lubrication forces introduced by the asperities contribute the tangential forces between the particles, hence increasing the viscosity.
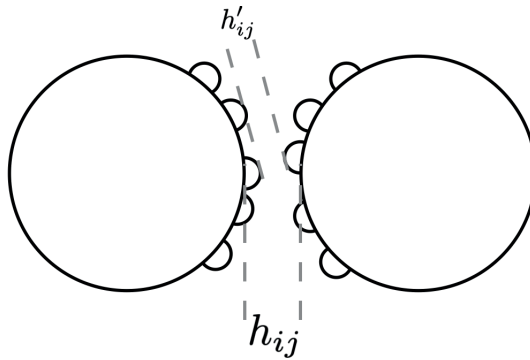
Figure 2.14: Sketch showing two rough particles at separation h_{ij}, and an extra separation h'_{ij} introduced by the asperities on the surfaces.

4 Oscillatory Rheology
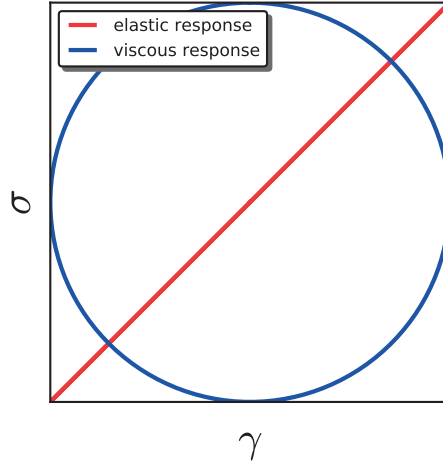
Figure 2.15: Schematic illustrations of Lissajous curve (shear stress as functions of strain) for elastic and viscous materials.

Oscillatory rheology is an experimental tool that is widely used to study mechanical properties of viscoelastic soft materials. A typical set-up places samples between two plates and applies a sinusoidal strain, $\gamma(t) = \gamma_0 \sin \omega t$ (the shear-rate is thus a cosine function), where γ_0 is the maximum strain and ω is the oscillation frequency. The time-dependent stress $\sigma(t)$ is then measured. Assuming linear rheology, the response of pure elastic and pure viscous materials can be expressed analytically,

$$\sigma(t) = G'\gamma_0 \sin(\omega t), \tag{2.48}$$

for elastic materials which is in-phase with strain, and

$$\sigma(t) = G''\gamma_0 \cos(\omega t), \tag{2.49}$$

for viscous materials which has a $\pi/2$ phase shift, where G' and G'' are the storage and loss modulus respectively. A schematic illustration of such behaviours is shown in Fig. 2.15. The straight line indicates that the shear stress is always in-phase with the strain while the circle indicates that the shear stress is always out-phase with the strain. The response of a viscoelastic material is a linear combination of Eqs. 2.48 and 2.49, $\sigma(t) = G'(\omega)\gamma_0 \sin(\omega t) + G''(\omega)\gamma_0 \cos(\omega t)$, where $G'(\omega)$ and $G''(\omega)$ both depend on oscillation frequency[63].

In addition to applications of viscoelastic materials, recent studies suggest that oscillatory shear can also alter behaviours of particle flows. It has been shown that by applying

an oscillatory cross shear to a primarily sheared flow (as demonstrated in Fig. 2.16), the viscosity of the flow drops, and hence flowability increases[64, 65]. Furthermore, the jamming packing fraction is found to be shifted to a higher value, *i.e.* a shear jammed suspension can start to flow (*i.e.* unjam)[65]. These behaviours are desired in many industrial applications. The mechanism behind this viscosity drop is not fully understood. Possible explanations consider the changes in microstructure of the suspensions caused by oscillation. It has been found that particles in the suspensions can have reversible trajectories in the cases of small oscillation magnitudes[66–68], suggesting that the particles are organised into an "absorbing state" where they are able to avoid contact with each other. The decrease of particle contact lowers the contact stress. Another possible explanation is that the oscillatory cross shear tilt and break the force chains and hence decrease the efficiency of stress transmission[64]. Fig. 2.17 shows a schematic illustration of how a force chain propagates through particles at contact.
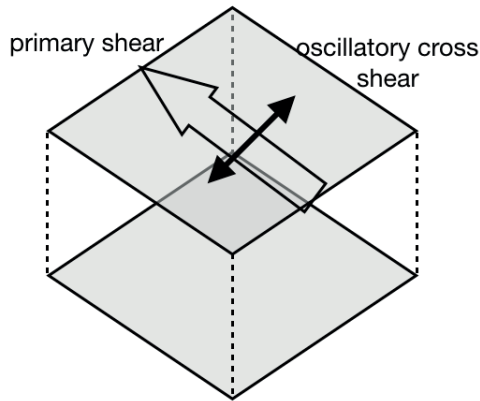
Figure 2.16: Demonstration of oscillatory cross shear of a primarily sheared flow.
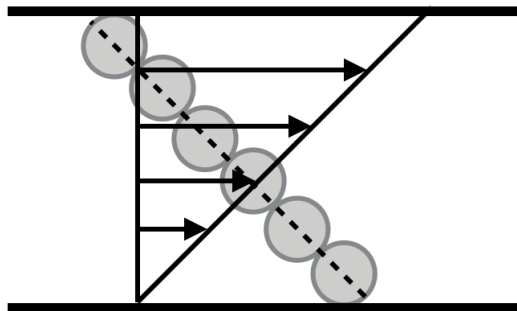
Figure 2.17: Schematic illustration of how a force chain (indicated by the dashed line) propagate through particles at contact under shear along the compressive axis.

To simulate the behaviour of granular flows, one solves equations that describe the dynamics of the system. As has been discussed in previous chapters, the motion of the particles is described by Newton's equations of motion, and the fluid is described by the Navier-Stokes equations. At the most detailed level, one solves these equations by imposing a no-slip condition on the boundary between the fluid and the particles as well as between fluid and the confining wall. This approach is computationally heavy and therefore not suitable for dense flows, where the number of particles is large.

In order to study large systems, approximations are necessary. One approach is to average out the fluid velocity, *i.e.* instead of solving for the fluid velocity at each point, the fluid is represented by a locally averaged velocity. The equations of motion for the particles remains to be solved separately. This approach is referred to as the discrete element method (DEM). Various versions of this method have been developed. One of them is Stokesian dynamics[69, 70]. In Stokesian dynamics, the hydrodynamic force (*i.e.* the force between the fluid and the particles) is given as

$$\mathbf{F}^b = -\overline{\overline{\mathbf{R}}}_{FU} \cdot (\mathbf{U}_p - \mathbf{u}^\infty) + \overline{\overline{\mathbf{R}}}_{FE} : \overline{\overline{\mathbf{e}}}, \tag{3.1}$$

where $\mathbf{U}_p$ is the particle velocity, $\mathbf{u}^\infty$ is the fluid velocity, $\overline{\overline{\mathbf{R}}}_{FU}$ and $\overline{\overline{\mathbf{R}}}_{FE}$ are two resistance matrices and $\overline{\overline{\mathbf{e}}}$ the strain-rate tensor. Stokesian dynamics gives a fairly accurate description of hydrodynamic forces for flows with small Reynolds number. Another approximation is to take a local average of both the fluid velocity, and the particle velocity. The equations of motion then look as for two continuous phases (or two imaginary fluids). This approach is thus referred to as the "two fluid model" and is mostly

used in continuum modelling/theory[71].

In this work, we used a discrete element method in two dimensions, where particles are circular discs. Hydrodynamics is described via a continuum approach. The main difference from Stokesian dynamics is that the averaging scale of the fluid is much larger than the particle size and the feedback of the particles on the fluid follows a mean-field approximation. This leads to a fluid velocity $\mathbf{u}^f = (y\dot{\gamma}, 0)$ being dependent only on the $y-$coordinate of the fluid, *i.e* the fluid velocity is constant along the $x-$coordinate for constant y. The time step dt is chosen so that it is smaller than the fastest characteristic time-scale in the system, *e.g.* among viscous relaxation, vibrations at the contacts, etc. More detailed descriptions of forces and dynamics are given below.
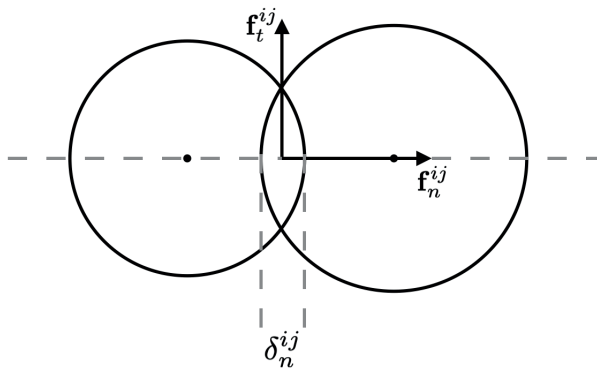
1   Forces

Figure 3.1: Sketch of two discs in contact with each other, with illustration of $\mathbf{f}_n^{ij}$ and $\mathbf{f}_t^{ij}$ as well as the overlap δ_n^{ij}.

1.1   Contact forces

As packing fractions are high in dense suspensions and granular flows, contact forces between colliding discs are dominating. The contact force is modelled by two damped harmonic springs, one for the normal force and one for the tangential force. For two colliding discs i and j, the contact force between them can be expressed as[30]

$$\mathbf{f}^{ij} = \mathbf{f}_n^{ij} + \mathbf{f}_t^{ij} = (k_n\delta_n^{ij} + \zeta_n\dot{\delta}_n^{ij})\mathbf{n}^{ij} + (k_t\delta_t^{ij} + \zeta_t\dot{\delta}_t^{ij})\mathbf{t}^{ij}, \qquad (3.2)$$

where k_n is the normal spring constant, ζ_n is the normal dissipation constant, δ_n^{ij} is the normal overlap between i and j as illustrated in Fig. 3.1, $k_t = k_n/2$ is the tangential spring constant and δ_t^{ij} is the relative tangential displacement between i and j as defined

in Eq. 3.3, ζ_t is the normal dissipation constant, $\mathbf{n}^{ij}$ denotes the normal unit vector and $\mathbf{t}^{ij}$ denotes the tangential unit vector, and the dots indicates a time derivative. In our simulations we ensure that the discs are non-deformable and rigid, *i.e.* $k_n/P \gg 1$ (in practice, we keep $k_n/P > 10^3$ [30]). Only overlaps between pairs of discs are considered here, and overlaps caused by multiple discs are neglected because they are very unlikely, due to the high rigidity of discs. Fig. 3.2 illustrate the overlap caused by three discs, which is marked black.
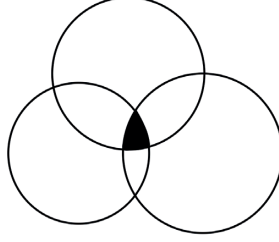
Figure 3.2: Sketch showing three discs in contact with each other, the overlap caused by the three discs are colored black.

The relative tangential displacement δ_t^{ij} is defined as

$$\delta_t^{ij} = \int_0^t u_t^{ij} dt, \tag{3.3}$$

where u_t^{ij} is the tangential projection of the relative velocity between i and j,

$$u_t^{ij} = \mathbf{t}^{ij} \cdot \mathbf{u}^{ij}, \tag{3.4}$$

where $\mathbf{u}^{ij}$ is the relative velocity. In addition, the tangential force is restricted by the Coulomb friction, *i.e.* the maximum value of $\mathbf{f}_t^{ij}$ is restricted by the corresponding $\mathbf{f}_n^{ij}$,

$$|\mathbf{f}_t^{ij}| \leq \mu_p |\mathbf{f}_n^{ij}|, \tag{3.5}$$

where μ_p is the particle friction coefficient, which reflects the surface properties of the discs. A typical value for μ_p is 0.4. For example surfaces of steel, glass, chromium, nylon-66 all have values around 0.4 [72].

The normal dissipation constant ζ_n is defined as,

$$\zeta_n = -\frac{2\sqrt{m_{ij}k_n}\ln e}{\sqrt{\pi^2 + (\ln e)^2}}, \tag{3.6}$$

where $m_{ij} = m_i m_j/(m_i + m_j)$ is the reduced mass. The restitution coefficient, e, describes the velocity difference before and after collision. The tangential dissipation

constant is defined similarly by replacing k_n in Eq. 3.6 with k_t. A dissipative collision can be intuitively illustrated by the trajectory of a bouncing ball, as shown in Fig. 3.3. A larger e indicates that less energy is dissipated during each collision, as seen by comparing red and black curves in Fig. 3.3. In the viscous regime, the contact force is balanced
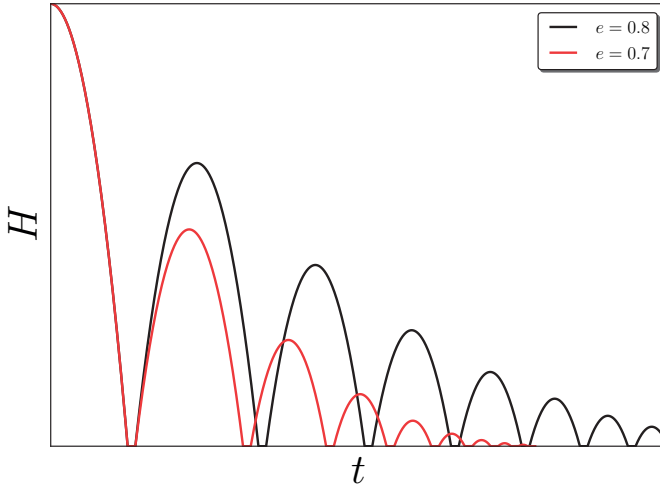
Figure 3.3: Schematic plot of the trajectory of a ball bouncing on hard surface with two restitution coefficient e.

by the viscous force and we have chosen to put $e = 1$ (*i.e.* no velocity loss in collisions), due to numerical reasons so that we can use a simple overdamped dynamics which only involves single particle velocities.

1.2 Viscous force

Apart from the contact force, the fluid also exerts forces on the discs. Hydrodynamic forces in suspensions of neutrally buoyant discs with packing fraction ϕ can be described by the two-phase flow Reynolds-averaged Navier-Stokes equations [48, 73],

$$\rho_f(1 - \phi)\frac{d\mathbf{u}^f}{dt} = \nabla \cdot \overline{\overline{\boldsymbol{\sigma}}}^f - \mathbf{F}, \tag{3.7}$$

where ρ_f is the fluid density, $\overline{\overline{\boldsymbol{\sigma}}}^f$ is the fluid stress tensor, and $\mathbf{F}$ is the total force between the fluid and the discs. Recalling that the fluid is Newtonian, Eq. 3.7 can be simplified to

$$\nabla \cdot \overline{\overline{\boldsymbol{\sigma}}}^f - \mathbf{F}^v = 0. \tag{3.8}$$

The force $\mathbf{F}^v$ is defined as the sum of the drag force and the Archimedes force over all discs i in volume V,

$$\mathbf{F}^v = \frac{1}{V} \sum_i (\mathbf{f}_i^{\text{drag}} + \mathbf{f}_i^{\text{Archi}}), \qquad (3.9)$$

where $\mathbf{f}_i^{\text{Archi}} = V_p \nabla \cdot \overline{\overline{\boldsymbol{\sigma}}}_i^f$, and V_p is the particle volume. Plugging Eq. 3.9 into Eq. 3.8 and using $V \approx V_p/\phi$,

$$\mathbf{f}_i^{\text{Archi}} \approx \frac{\phi}{1-\phi} \mathbf{f}_i^{\text{drag}}. \qquad (3.10)$$

Combining Eq. 3.9 and 3.10, we derive

$$\mathbf{F}^v = \sum_i \mathbf{f}_i^v = \frac{1}{1-\phi} \sum_i \mathbf{f}_i^{\text{drag}}. \qquad (3.11)$$

The viscous drag $\mathbf{f}_i^{\text{drag}}$ in two dimensions is given by reformulating Eq. 2.27,

$$\mathbf{f}_i^{\text{drag}} = 3\pi\eta_f(\mathbf{u}^f - \mathbf{u}_i^p), \qquad (3.12)$$

where $\mathbf{u}^f$ is the fluid velocity and $\mathbf{u}^p$ is the disc velocity. The viscous torque can be calculated similarly, with

$$\boldsymbol{\tau}_i^{\text{drag}} = \pi\eta_f(\boldsymbol{\omega}^f - \boldsymbol{\omega}_i^p), \qquad (3.13)$$

where $\boldsymbol{\omega}^f = \dot{\gamma}/2$ is the angular velocity of the fluid and $\boldsymbol{\omega}^p$ is the angular velocity of the disc. Besides viscous drag, the discs are also subjected to pair lubrication forces. Here we use a regularised lubrication model to compute the force. A schematic plot of this force is seen in Fig. 2.12. The equations used for computing lubrication forces between disc i and j are[48, 74]

$$\mathbf{f}_{\text{lub,n}}^{ij} = \left[-\frac{3}{8}\pi\eta_f d_{ij} \frac{(\mathbf{v}_i - \mathbf{v}_j) \cdot \mathbf{n}_{ij}}{h_{ij} + \Delta} \right] \mathbf{n}_{ij}, \qquad (3.14)$$

$$\mathbf{f}_{\text{lub,t}}^{ij} = \left[-\frac{1}{2}\pi\eta_f \ln\left(\frac{d_{ij}}{2(h_{ij} + \Delta)}\right)(\mathbf{v}_i - \mathbf{v}_j) \cdot \mathbf{t}_{ij} \right] \mathbf{t}_{ij}, \qquad (3.15)$$

where $\mathbf{f}_{\text{lub,n}}^{ij}$ is the normal lubrication force and $\mathbf{f}_{\text{lub,t}}^{ij}$ is the tangential lubrication force, h_{ij} is the gap between the two discs i and j, $\mathbf{v}_i$ and $\mathbf{v}_j$ are the velocities of discs i and j at the closest points, $d_{ij} = 2d_i d_j/(d_i + d_j)$ and Δ is the regularisation length, related to the roughness of the particles. The torque exerted on disc i from lubrication forces between disc i and j is

$$\boldsymbol{\tau}_i^{\text{lub}} = \mathbf{f}_{\text{lub,t}}^{ij} \times \mathbf{r}_i \qquad (3.16)$$

where $\mathbf{r}_i$ the position vector of particle i.

2 Dynamics

2.1 Equation of motion

Particle dynamics in a fluids can be described by Newton's equation of motion [7]

$$m_i \frac{d\mathbf{u}_i}{dt} = \mathbf{f}_i^v + \mathbf{f}_i^{ext} + \sum_j \mathbf{f}_{ij}^c, \tag{3.17}$$

where $\mathbf{f}_i^v$ is the viscous force depending on the position and the velocity of the particle, $\mathbf{f}_i^{ext}$ is the external force and $\mathbf{f}_{ij}^c$ is the contact force, both depending on the current position of the particle. The particle positions and velocities can be calculated by integrating Eq. 3.17, using the Verlet algorithm[75] (note that Verlet algorithm is not used for the suspensions in the viscous regime, where we have overdamped Langevin dynamics instead, as discussed in the next section),

$$\mathbf{r}_i(t + \Delta t) = 2\mathbf{r}_i(t) - \mathbf{r}_i(t - \Delta t) + \frac{1}{m_i}\left(\mathbf{f}_i^v(t) + \mathbf{f}_i^{ext}(t) + \sum_i \mathbf{f}_{ij}(t)\right)\Delta t^2, \tag{3.18}$$

$$\mathbf{u}_i(t + \Delta t) = \frac{\mathbf{r}_i(t + \Delta t) - \mathbf{r}_i(t - \Delta t)}{2\Delta t} + \frac{1}{m_i}\left(\mathbf{f}_i^v(t) + \mathbf{f}_i^{ext}(t) + \sum_i \mathbf{f}_{ij}(t)\right)\Delta t, \tag{3.19}$$

where $\mathbf{u}_i(t + \Delta t)$ and $\mathbf{r}_i(t + \Delta t)$ are the new velocity and position, $\mathbf{r}_i(t)$ is the current position, and $\mathbf{r}_i(t - \Delta t)$ is the old position, and Δt is the time step. Similar equations are used for the angular velocity using the moment of inertia for the discs.

2.2 Overdamped Langevin dynamics

In the viscous regime, particle dynamics are strictly overdamped which gives force and torque balance [76]

$$\mathbf{f}_i^{ext} + \mathbf{f}_i^v + \sum_j \mathbf{f}_{ij} = 0, \tag{3.20}$$

$$\boldsymbol{\tau}_i^{ext} + \boldsymbol{\tau}_i^v + \sum_j \boldsymbol{\tau}_{ij} = 0. \tag{3.21}$$

where $\mathbf{f}_i^{ext}$ is the external force, $\mathbf{f}_i^v$ is the viscous force, the sum of which is given by Eq. 3.11, and $\mathbf{f}_{ij}$ is the contact force given by Eq. 3.2. $\boldsymbol{\tau}_i^{ext}$, $\boldsymbol{\tau}_i^v$ and $\sum_j \boldsymbol{\tau}_{ij}$ are torques resulting from external, viscous and contact forces respectively. The external force $\mathbf{f}_i^{ext}$ in sheared suspensions comes from walls, so for particles in bulk we have

$$\mathbf{f}_i^v = -\sum_j \mathbf{f}_{ij}. \tag{3.22}$$

Combining with Eq. 3.12, the velocity of the particle can be calculated assuming no external forces

$$\mathbf{u}_i(t) = \mathbf{u}^f - \frac{(1-\phi)}{3\pi\eta_f} \sum_j \mathbf{f}_{ij}(t),$$ (3.23)

and the position of the particles is calculated from

$$\mathbf{r}_i(t + \Delta t) = \mathbf{r}_i(t) + \mathbf{u}_i(t)\Delta t.$$ (3.24)

The angular velocity is calculated similarly for the torque.

3   Models for frictional contacts

As we have discussed in section 3.5, DST can be explained by an "activation" of frictional contacts. In order to reproduce DST behavior in simulations, we introduce the *Critical Load Model* (CLM) in our simulations [45, 53, 58]. CLM describes the friction coefficient between particle i and j, μ_p^{ij}, as a step function,

$$\mu_{\mathrm{p}}^{ij} = \begin{cases} \mu_p, & |\mathbf{f}_{\mathrm{n}}^{ij}| \geq f_{\mathrm{n}}^{\mathrm{cl}}; \\ 0, & |\mathbf{f}_{\mathrm{n}}^{ij}| < f_{\mathrm{n}}^{\mathrm{cl}}, \end{cases}$$ (3.25)

where $\mathbf{f}_{\mathrm{n}}^{ij}$ is the normal force between i and j and $f_{\mathrm{n}}^{\mathrm{cl}}$ is a threshold force which represents the repulsive layer around particles. According to CLM, contacts between two particles are frictional only when the normal force overcomes the threshold force; otherwise, contacts are non-frictional. While CLM is computationally fast, it neglects the length scale of repulsive layers. Such an approximation is reasonable since the size of repulsive layer usually is much smaller than the size of the particles. Contacts are defined as frictional if $\mu_{\mathrm{p}}^{ij} = \mu_p$, and non-frictional if $\mu_{\mathrm{p}}^{ij} = 0$. The fraction of frictional contacts is defined as $\chi_f = Z_f/Z$, where Z_f is the average number of frictional contacts and Z is the average total number of contacts.

In order to closely investigate the role of the fraction of frictional contacts χ_f in suspension rheology, we design an ideal suspension consisting of a binary mixture of rough discs (*i.e.* $\mu_p^i = \mu_p$) and ideally smooth discs (*i.e.* $\mu_p^i = 0$). The friction coefficient between particles i and j is $\mu_p^{ij} = \sqrt{\mu_p^i \mu_p^j}$, which we call the *binary model*. Clearly, only contacts between two rough particles are frictional. The fraction of frictional contacts χ_f can therefore be well-controlled by adjusting the amount of rough discs in the system. We use the binary model here as a toy model, for a better understanding of the role of the fraction of frictional contacts, in macroscopic rheology of suspensions.

4 Simulation details
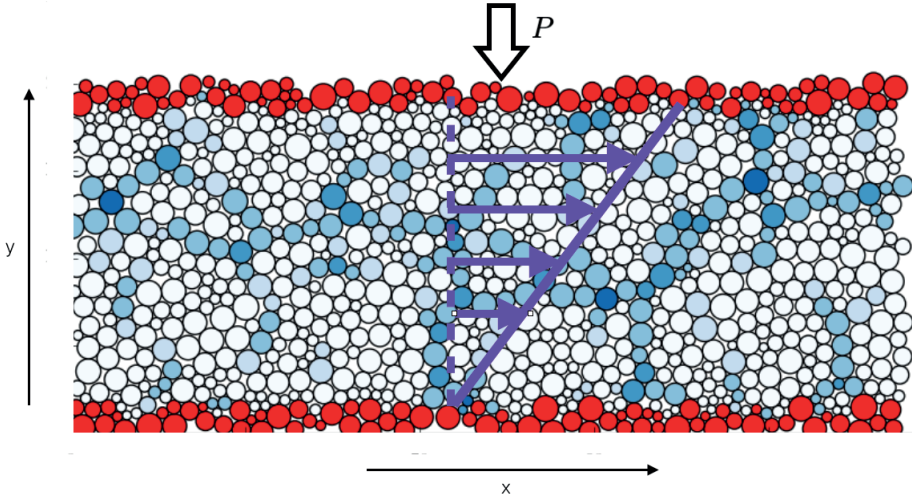
Figure 3.4: A snapshot from simulations; the black arrow indicates the imposed pressure and purple arrows describe fluid the velocity profile.

Fig. 3.4 is a snapshot taken form an actual simulation. We use it here to illustrate our simulation box. The simulation box contains roughly 1000 circular discs. The disc diameters are described by a flat distribution with $\pm 50\%$ polydispersity with average diameter d. All lengths in the simulations are in units of d. The walls consist of the same types of discs as in the suspension but glued together. Wall particles are marked red in Fig. 3.4. For simulations with constant imposed pressure, the bottom wall is fixed and the top wall is adjustable with an imposed pressure P along the $y-$axis, which balances the normal stress along the $y-$axis at steady state. For simulations with constant packing fraction, both walls are fixed along the $y-$axis. For simulations with steady shear, the top wall moves at constant velocity along the $x-$axis, resulting in a strain of the suspension with constant strain rate. For simulations with oscillation, an additional oscillatory function along the $x-$axis is applied to the top wall, resulting an oscillating shear-rate $\dot{\gamma} = \dot{\gamma}_0 + \dot{\gamma}_1 \cos(\omega t)$. We define $\mathcal{F} = \dot{\gamma}_1/\dot{\gamma}_0$ as the magnitude of oscillation and $\mathcal{G} = \gamma_1 = \dot{\gamma}_1/\omega$ as the maximum strain caused by oscillation. The fluid is simulated as a continuum velocity profile, with a no-slip boundary at the walls. The velocity profile is illustrated by purple lines in Fig. 3.4. Periodic boundary conditions are applied along the x-axis, and the interaction between discs is calculated following the nearest image convention, as illustrated in Fig. 3.5.
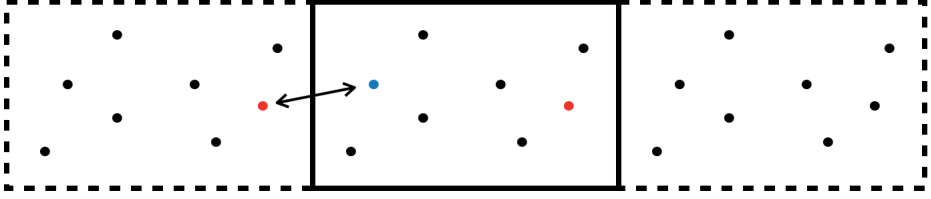
Figure 3.5: Sketch of a simulation box (as represented by the rectangle with solid lines) and its two neighbor images (dashed lines). The interaction between the blue and red discs in the simulation box is considered by calculating the interaction between the blue and red disc in the neighboring image box, as indicated by the arrow.

Shear stress σ_{xy} and pressure $P = \sigma_{yy}$ are calculated from the particle stress tensor

$$\overline{\overline{\sigma}}_p = \frac{1}{A} \sum_{i \in A} \mathbf{f}_i \cdot \mathbf{r}_i = \begin{bmatrix} \sigma_{xx} & \sigma_{xy} \\ \sigma_{yx} & \sigma_{yy} \end{bmatrix}, \tag{3.26}$$

where A is the area over which stresses are sampled, $\mathbf{f}_i$ is the total force acting on disc i; $\sigma_{xy} = \sigma_{yx}$ is the shear stress, and σ_{xx} and σ_{yy} are the normal stresses along the $x-$ and $y-$axis respectively. The reported values are ensemble averages, calculated from the values that are sampled throughout the simulations. Before sampling, a pre-shear protocol is run to ensure that we sample from the steady state of the suspensions. In case of constant shear-rate, shear strain γ is always kept larger than 3, in order to guarantee sufficient sampling. In case of oscillation, sampling is either over at least 10 oscillation periods, or a minimum absolute shear strain over 10.

1 Paper 1: Analog of discontinuous shear thickening flows under confining pressure

In Paper 1, we focus on dense suspensions in the viscous regime, under pressure-imposed shear. The particle friction coefficient $\mu_p = 1$. We first investigate suspensions with the binary model, where the fraction of frictional contacts χ_f is well-controlled, and show that the fraction of frictional contacts χ_f needs to be included into the constitutive law, to characterise such suspensions,

$$\phi = \phi(J, \chi_f), \tag{4.1}$$

$$\eta/\eta_f = g(\phi, \chi_f). \tag{4.2}$$

Eq. 4.1 and 4.2 are used to describe suspensions with the Critical Load Model (CLM), where χ_f is allowed to adapt during simulations. Therefore, an extra constitutive law is introduced to characterise χ_f,

$$\chi_f = \chi_f(\hat{f}, J), \tag{4.3}$$

where $\hat{f} = f_n^{cl}/(Pd)$ is a dimensionless threshold force. Two shear protocols are employed during the simulations; the first one decreases J by keeping the pressure P constant and gradually decrease the shear-rate $\dot{\gamma}$, the second one decreases J by keeping the shear-rate $\dot{\gamma}$ constant and gradually increasing pressure P. For shear protocols with constant P, continuous flow curves between two branches are observed, while for the constant $\dot{\gamma}$ shear protocol, cusped curves are observed, as illustrated in Fig. 4.1. This
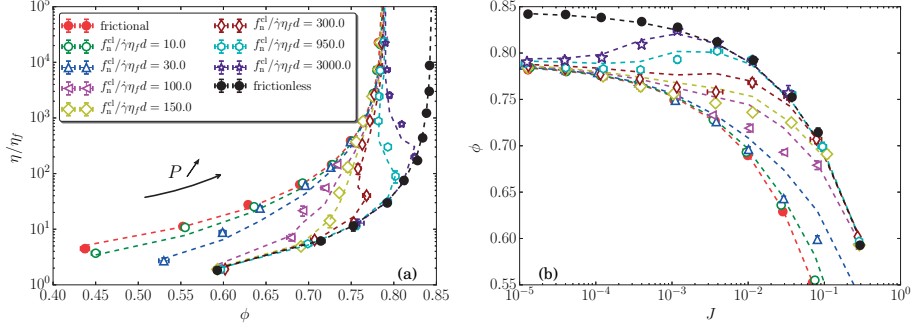
Figure 4.1: Flow curves of dense suspensions in viscous regime with constant $\dot{\gamma}$ shear protocol; symbols are simulation results and dashed lines are plots of Eq. 4.1 and 4.2.

indicates a negative dynamic compressibility. Such behaviors can be explained by the fact that χ_f increases with P, resulting in higher particle pressure, which will expand the suspension.
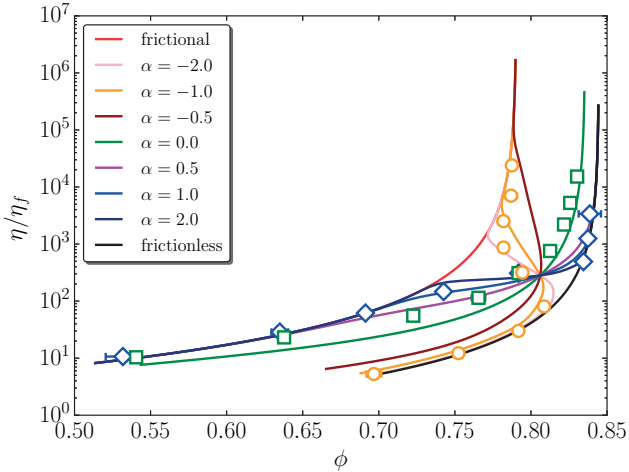
Figure 4.2: Viscosity η/η_f as a function of packing fraction ϕ for various α with $J_0 = 0.001$, $D = 1$ (defined in Eq. 4.4); frictional and frictionless curves are produced by setting $D = 0$ and ∞, symbols are simulation results for $\alpha = -1$ (circles), 0 (squares), and 1 (diamonds).

Furthermore, we express the difference shear protocols by a combination of $\hat{f}$ and J. A constant P shear protocol can be expressed as keeping $\hat{f}J^0$ constant. Similarly, a constant $\dot{\gamma}$ shear protocol can be expressed as constant $\hat{f}J^{-1}$. To unify these two shear

protocols, we construct a new dimensionless parameter,

$$D = \hat{f}\left(\frac{J}{J_0}\right)^\alpha, \qquad (4.4)$$

where J_0 is a rescaling constant giving the inflection point, as α varies. D and α encode the magnitude of the threshold force and the different shear protocols. Fig. 4.2 shows analytical predictions of flow curves using Eq. 4.1 and 4.3. Different transition pathways are observed. Simulation results of three corresponding cases are plotted with good agreement with analytical prediction.

In addition, we run a few simulations with a "softer" CLM model, *i.e.* a linear function that saturates when $|f_n^{ij}| \geq f_n^{cl}$,

$$\mu_p^{ij} = \begin{cases} \mu_p, & |\mathbf{f}_n^{ij}| \geq f_n^{cl}; \\ \frac{\mu_p f_n^{ij}}{f_n^{cl}}, & |\mathbf{f}_n^{ij}| < f_n^{cl}. \end{cases} \qquad (4.5)$$

Results are plotted in Fig. 4.3. Similar cusped curves can be seen with a smaller curvature, compared with the curves in Fig. 4.1(a).

Figure 4.3: Viscosity η/η_f as a function of packing fraction ϕ with μ_p^{ij} described by Eq. 4.5.

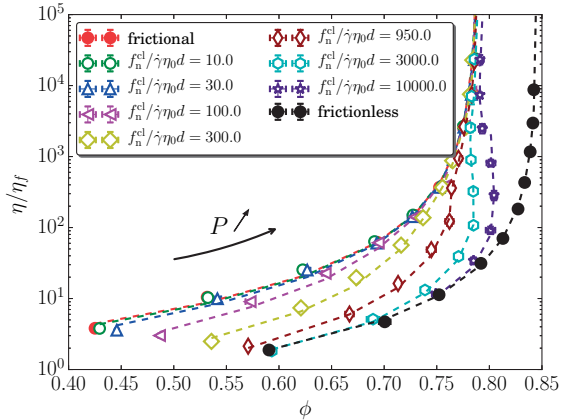## 2 Paper II: Unifying viscous and inertial regimes of discontinuous shear thickening suspensions

In Paper II, we extend our findings in Paper I, and present unified constitutive laws for discontinuous shear thickening suspensions spanning from the viscous to inertia regimes (*i.e.* $I/J \in [0, \infty]$). The particle friction coefficient μ is set to 0.4 when they are frictional in this paper. The general idea of the unification is that the shear stress σ_{xy} and the pressure P can be expressed as linear combinations of viscous and inertial contributions, as shown in Eqs. 2.41 and 2.42 in Chapter 2. For the friction and packing fraction laws, we employ phenomenological expressions

$$\phi = \phi_c - a_\phi K^n, \tag{4.6}$$

$$\mu = \mu_c + a_\mu K_\mu^n, \tag{4.7}$$

where $K = J + \alpha I^2$, $K_\mu = J + \alpha_\mu I^{\gamma_\mu}$, and α, α_μ, n, γ_μ are all empirical parameters, which are χ_f-dependent. In the frictional case, $\gamma_\mu = 2$ so that $g_{J,\sigma}$ and $g_{I,\sigma}$ (introduced in Eq. 2.11 and 2.35) share the same exponent of divergence, and one has $g_{J,\sigma} = g_{I,\sigma}/\alpha$. In the frictionless case, $\gamma_\mu = 1$, which lead to different exponents of divergence between $g_{J,\sigma}$ and $g_{I,\sigma}$ and thus $g_{I,\sigma}/g_{J,\sigma}$ becomes ϕ-dependent. However, we find that as $\phi \to \phi_c$, one gets $g_{I,\sigma} \to \alpha g_{J,\sigma}$. As ϕ gets smaller, $g_{I,\sigma}$ deviates from $\alpha g_{J,\sigma}$. In the dense regime, this difference is small , as shown in Fig. 4.4. Hence, we can approximate $g_{I,\sigma} \approx \alpha g_{J,\sigma}$ for the frictionless case.
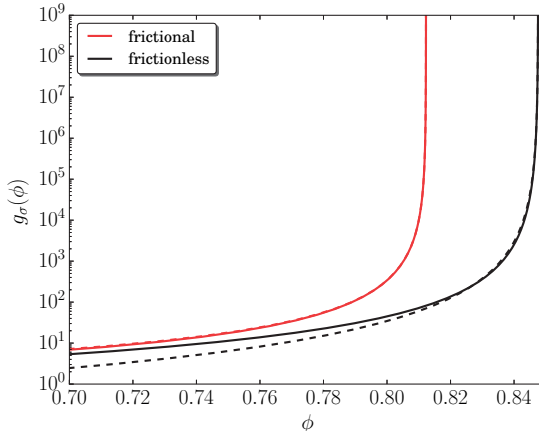

Figure 4.4: Plots of $\alpha g_{J,\sigma}$ (solid lines) and $g_{I,\sigma}$ (dashed lines) for the frictional ($\mu_p = 0.4$, red lines) and the frictionless cases ($\mu_p = 0$, black lines).

Values of all empirical parameters and their dependence on χ_f, are extracted from the binary model. Furthermore, it is found that χ_f can be characterised by $\hat{f}Z$. As
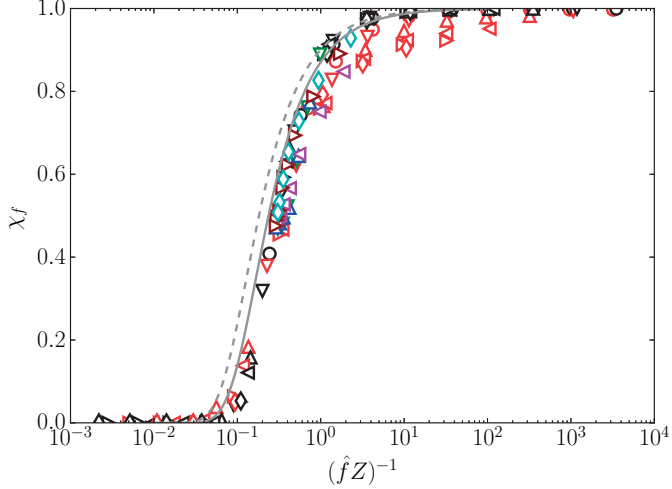
Figure 4.5: Values of χ_f at different $(\hat{f}Z)^{-1}$ for suspensions with various I/J; red symbols are simulation results for viscous suspensions ($I/J = 0$), black symbols are simulation results for inertial suspensions ($I/J = \infty$), symbols with other colors are results with finite I/J; the solid line and the dashed line are plots of $\chi_f = 1 - \tanh(k \cdot \hat{f}Z)$ with $k = 0.13$ for the solid line and $k = 0.08$ for the dashed line.

seen in Fig. 4.5, χ_f for various I/J collapse to a master curve, when plotted as a function of $(\hat{f}Z)^{-1}$. The derived constitutive laws are applied to simulation data obtained from CLM. Figs. 4.6 and 4.7 show behaviours of dense suspensions with different I/J. Fig. 4.6 shows the cases of the fully frictional, and fully frictionless, and Fig. 4.7 shows the cases with $\hat{f} = 1$. A good collapse between data with different I/J is observed in all the cases, indicating that our unification is valid. The dashed lines are the plots of the constitutive laws, which show a good agreement with the simulation result.

We further generalise the D parameter that we have introduced in Paper 1 to

$$F = \hat{f}\left(\frac{K}{K_0}\right)^\epsilon. \tag{4.8}$$

Similarly, ϵ encode different shear protocols and K_0 is a constant that gives the intersection point as ϵ varies (*i.e.* the point where curves for different shear protocols intersect). In Fig. 4.8, we present analytical predictions of $g_{J,\sigma}$ with different ϵ, together with simulation data for $\epsilon = -1, 0$ and 1, and different I/J. In Fig. 4.9 we furthermore show that our constitutive laws are able to reproduce typical shear thickening behaviours, under constant ϕ. Fig. 4.9(a) shows predictions of $g_{J,\sigma}$ (or equivalently the rescaled viscosity in the viscous regime) under constant ϕ. The increase in viscosity becomes more drastic as ϕ increases. Fig. 4.9(b) and (c) show the cases where shear thickening happens at intermediate and high Stokes number, respectively. In Fig. 4.9(b), the suspensions start in the viscous regime where the viscosities remain constant, then undergo discontinu-

ous shear-thickening and enter the inertial regime where the viscosities increase linearly with the shear-rate. In Fig. 4.9(c) the suspensions are always in the inertial regime so that the viscosities increase linearly with the shear-rate, before and after discontinuous shear-thickening.
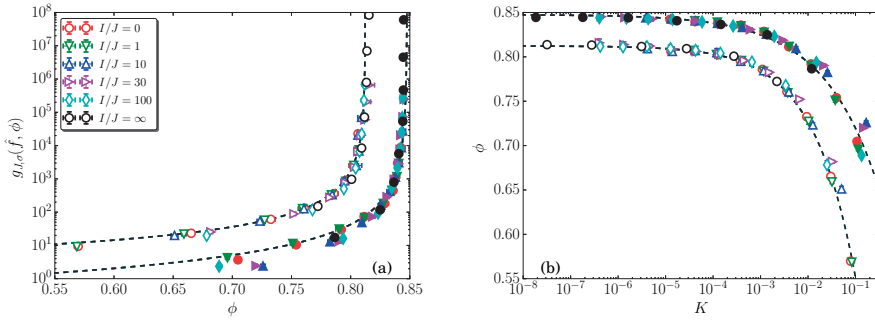
Figure 4.6: Rescaled viscosity $g_{J,\sigma}$ as functions of ϕ and (b) ϕ as function of K for frictional (empty symbols) and frictionless (filled symbol) suspensions with various I/J as indicated by legends. Symbols are simulation results and dashed lines are plots of the constitutive laws.
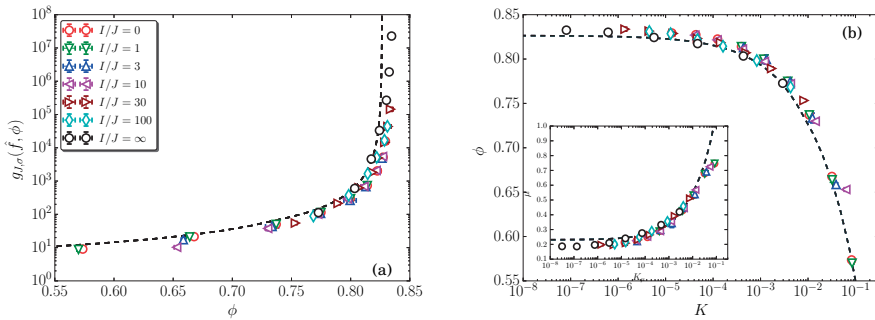
Figure 4.7: Rescaled viscosity $g_{J,\sigma}$ as functions of ϕ and (b) ϕ as function of K, in the inset μ as functions of K_μ for suspensions with $\hat{f} = 1$ and various I/J as indicated by legends. Symbols are simulation results and dashed lines are plots of the constitutive laws.
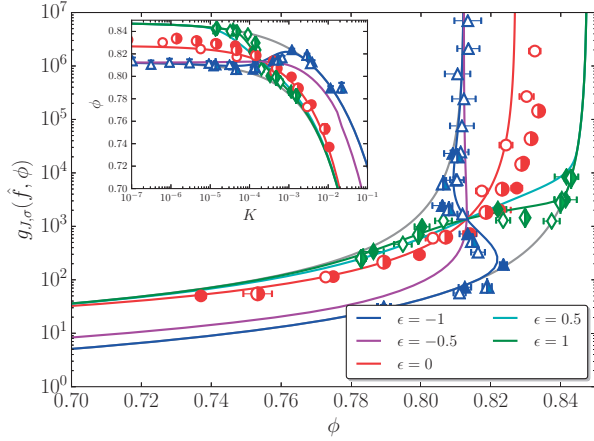
Figure 4.8: Analytical predictions of $g_{J,\sigma}$ as functions of ϕ for suspensions with $F = 1$ and various ϵ as indicated by legends. Symbols are simulation results: red circles corresponds to $\epsilon = 0$, blue triangles correspond to $\epsilon = -1$, green diamonds corresponds to $\epsilon = 1$; the filled symbols correspond to the viscous regime ($I/J = 0$), the empty symbols the inertia regime ($I/J = \infty$) and the half-filled symbols $I/J = 30$. In the inset, plots of ϕ as functions of K.
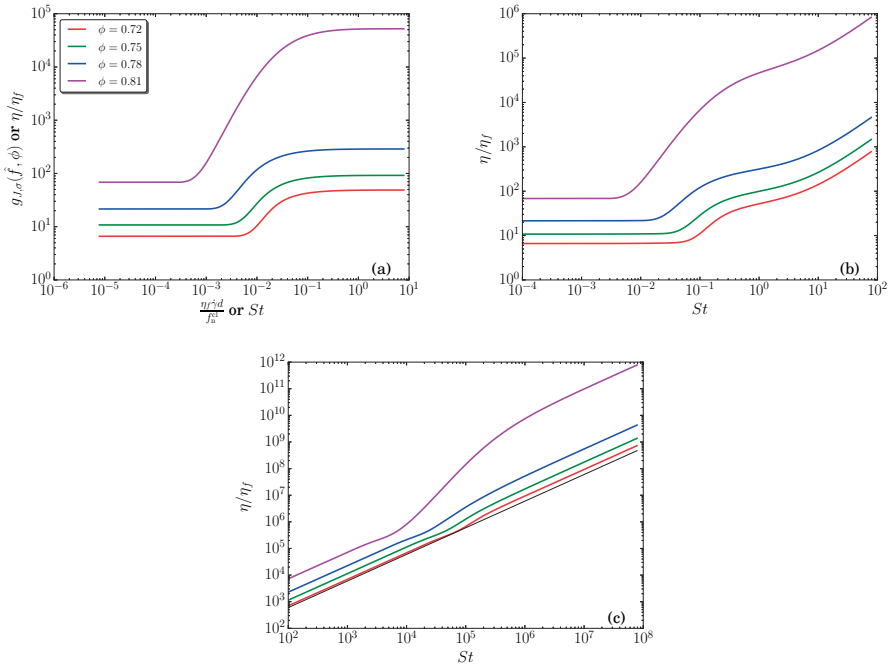
Figure 4.9: Analytical prediction of (a) $g_{J,\sigma}$ as functions of rescaled shear-rate $\eta_f \dot{\gamma} d / f_n^{c1}$, and rescaled viscosity η / η_f as functions of Stokes number with (b) intermediate Stokes number and (c) large Stokes number for suspensions under constant packing fraction.

3 Paper III: Transition from steady shear to oscillatory shear rheology of dense suspensions

In Paper III, we move from the case where we have constant shear-rate to the cases, where we have oscillating shear, *i.e.* $\dot{\gamma}(t) = \dot{\gamma}_0 + \dot{\gamma}_1 \cos(\omega t)$. We studied the behaviour viscous suspensions composed of either frictional ($\mu_p = 0.4$) or frictionless ($\mu_p = 0$) particles, under oscillating shear with $\mathcal{F} = \dot{\gamma}_1/\dot{\gamma}_0 \in [3 \cdot 10^{-2}, 3 \cdot 10^2]$ and $\mathcal{G} = \omega/\dot{\gamma}_1 \in [10^{-2}, 10]$. At constant shear-rate, the viscosity can be obtained as $\eta_\sigma = \langle\sigma\rangle/\langle\dot{\gamma}\rangle$, which we later refer to as the "stress" viscosity. This expression, however, becomes inaccurate as $\mathcal{F} \to \infty$ since $\langle\sigma\rangle \to 0$ and $\langle\dot{\gamma}\rangle \to 0$. For pure oscillatory shear flows, and assuming only viscous response, the viscosity can be calculated from

$$\eta' = \frac{\int_0^{2\pi/\omega} \sigma(t)\cos(\omega t)dt}{\dot{\gamma}_1 \int_0^{2\pi/\omega} \cos^2(\omega t)dt} = G''/\omega, \qquad (4.9)$$

where $G'' = \frac{\omega^2}{\pi\dot{\gamma}_1} \int_0^{2\pi/\omega} \sigma(t)\cos(\omega t)dt$ is the loss modulus[77]. In order to deal with shear flows, which are combinations of a steady shear and an oscillating shear, we generalise this equation and define shear-rate-averaged quantities as

$$\langle A \rangle_{|\dot{\gamma}|} = \frac{\int_0^{2\pi n/\omega} |A(t)||\dot{\gamma}(t)|dt}{\int_0^{2\pi n/\omega} |\dot{\gamma}(t)|dt}, \qquad (4.10)$$

where $A(t)$ is a time-dependent property, such as the shear stress σ_{xy}, or the number of contacts Z. The integer n is the number of oscillation periods that are averaged over. The shear-rate-averaged viscosity is then calculated as $\eta_{|\dot{\gamma}|} = \langle\sigma\rangle_{|\dot{\gamma}|}/\langle\dot{\gamma}\rangle_{|\dot{\gamma}|}$.

We first check how the instantaneous viscosities varies, and compare different viscosity definitions, as shown in Fig. 4.10. We can see in Fig. 4.10(a) that at small $\mathcal{F}$, the instantaneous viscosities show only slight fluctuations around the average, which equals the viscosities at constant shear-rate. The different viscosity definitions gives approximately the same values. At large $\mathcal{F}$, on the other hand, the instantaneous viscosities display two distinct and alternating viscosity peaks in each period, which are well-correlated with the peaks in strain as seen in Fig. 4.10(b). We can see that $\eta_{|\dot{\gamma}|}$ in general performs better in describing viscosities of suspensions under oscillation, and is closer to the time-averaged viscosity $\overline{\eta} = \omega \int_0^{2\pi n/\omega} \eta(t)dt/(2\pi n)$.

We then study how $\eta_{|\dot{\gamma}|}$ will vary at different $\mathcal{F}$ and $\mathcal{G}$ for a constant ϕ. We find that the viscosities start to decrease at $\mathcal{F} > 1$. The decrease is more significant for small $\mathcal{G}$. Moreover, at large $\mathcal{F}$ and small $\mathcal{G}$, the viscosities decrease to zero, as seen in Fig. 4.11(a). At $\mathcal{F} < 1$, on the other hand, the viscosities are close to the value at constant shear-rate, regardless of $\mathcal{G}$ values. Comparing Fig. 4.11(a) and (b), we can see that the decrease in
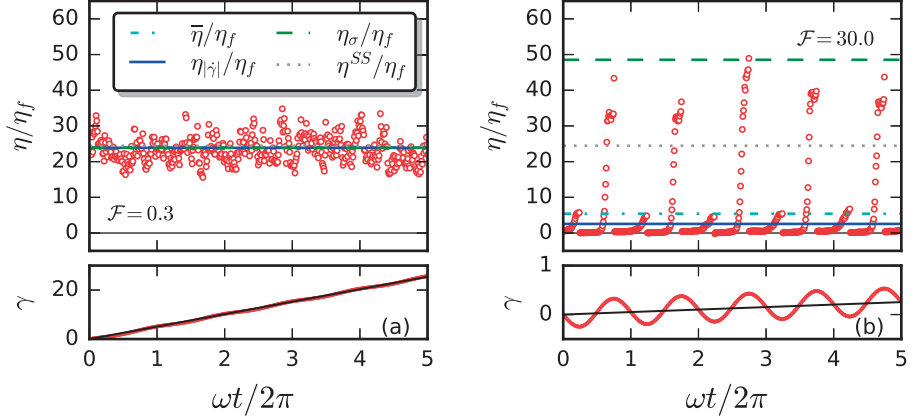
Figure 4.10: Instantaneous rescaled viscosities at $\phi = 0.67$, $\mu_p = 0.4$, $\mathcal{G} = 0.33$ and (a) $\mathcal{F} = 0.3$, (b) $\mathcal{F} = 30$. Lines with different colors and styles correspond to different definition of viscosity, as indicated in the legends. Thin black lines indicate $\eta/\eta_f = 0$. The rectangular plots beneath the main figures show how strain evolves under oscillatory shear; black lines show how strain would evolve with a constant shear-rate $\dot{\gamma}_0$.

viscosity is in agreement with the decrease in the number of contacts, indicating that the former is a consequence of the latter. The behaviour of the viscosity, and the number of contacts, can be described by a phenomenological hyperbolic tangent function,

$$A_{|\dot{\gamma}|}/A^{SS} = 1 - c_1 \tanh(c_2\mathcal{F}), \tag{4.11}$$

where A is either $\eta_{|\dot{\gamma}|}$ or $Z_{|\dot{\gamma}|}$, $c_1 = 1 - A_{|\dot{\gamma}|}^{\mathcal{F}=\infty}/A^{SS}$ and c_2 are fitting parameters.

Figure 4.11: (a) Rescaled viscosity $\eta_{|\dot{\gamma}|}/\eta^{SS}$, (b) $Z_{|\dot{\gamma}|}/Z^{SS}$ as function of $\mathcal{F}$ at various $\mathcal{G}$, $\phi = 0.76$ and $\mu_p = 0.4$. η^{SS} and Z^{SS} are values at constant shear-rate. Symbols are simulation results and dashed lines are best fits of Eq. 4.11.

We further define the viscous number and macroscopic friction for suspensions under
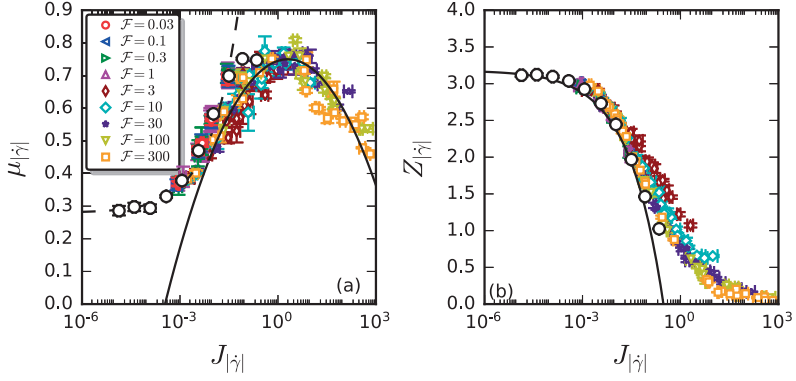
Figure 4.12: (a) Flow curves with extended $\mu(J)$-rheology for frictional suspensions ($\mu_p = 0.4$). (b) Number of contacts Z for either frictional (empty symbols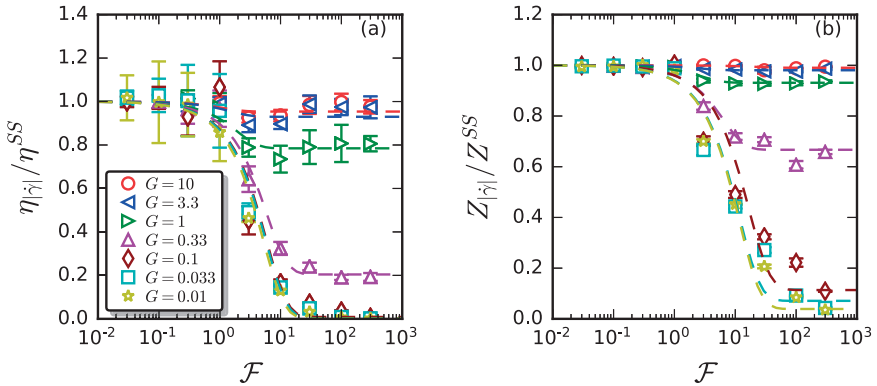) and frictionless suspensions (filled symbols). Black symbols correspond to values at constant shear-rate ($\mathcal{F} = 0$) while coloured symbols correspond to different $\mathcal{F}$ as indicated in the legends, with $\phi \in [0.67, 0.79]$.

oscillatory shear as $J_{|\dot\gamma|} = \eta_f \langle \dot\gamma / P \rangle_{|\dot\gamma|}$ and $\mu_{|\dot\gamma|} = \langle \sigma / P \rangle_{|\dot\gamma|}$. The results are plotted in Fig. 4.12, where we find data collapses in both $\mu(J)$ and $Z(J)$. As seen in Fig. 4.12(a), data points at $\mathcal{F} < 1$ are well described by the original $\mu(J)$-rheology at constant shear-rate. Data points for $\mathcal{F} > 1$ are better described by an empirical relation $\mu_{|\dot\gamma|} \simeq$

$\mu^{\mathrm{max}} - \kappa \left(\ln(J_{|\dot\gamma|}) - \ln(J_{|\dot\gamma|,0}) \right)^2$, with $\mu^{\mathrm{max}} \simeq 0.75$, $J_{|\dot\gamma|,0} \simeq 2$, and $\kappa = 0.01$, shown as solid black lines in Fig. 4.12(a). Fig. 4.12(b) shows plots of $Z(J)$, where we see a slightly better collapse.

4 Paper IV: Oscillatory shear flows of dense suspensions at imposed pressure

In this work, we focus on the behaviours of dense suspensions under pure oscillatory shear, *i.e.* $\dot{\gamma} = \dot{\gamma}_0 \cos(\omega t)$ and $\gamma = \gamma_0 \sin(\omega t)$, where $\dot{\gamma}_0$ is the shear-rate magnitude, $\gamma_0 = \dot{\gamma}_0/\omega$ the strain magnitude and ω the oscillation frequency. The particles of the suspensions are confined between two walls by a constant pressure, and are either frictional ($\mu_p = 0.4$) or frictionless ($\mu_p = 0$). For suspensions that display linear viscoelastic response, the shear stress can be expressed as

$$\sigma = \eta' \dot{\gamma}_0 \cos(\omega t) + \eta'' \dot{\gamma}_0 \sin(\omega t), \tag{4.12}$$

where

$$\eta' = \frac{\int_0^{2\pi/\omega} \sigma(t) \cos(\omega t) dt}{\dot{\gamma}_0 \int_0^{2\pi/\omega} \cos^2(\omega t) dt}, \tag{4.13}$$

$$\eta'' = \frac{\int_0^{2\pi/\omega} \sigma(t) \sin(\omega t) dt}{\dot{\gamma}_0 \int_0^{2\pi/\omega} \sin^2(\omega t) dt}, \tag{4.14}$$

and $|\eta^*| = \sqrt{\eta'^2 + \eta''^2}$ is the magnitude of the complex viscosity. Following the same generalisation approach as in Paper III, we define

$$\mu' = \frac{\int_0^{2\pi/\omega} (\sigma/P) \dot{\gamma} dt}{\int_0^{2\pi/\omega} |\dot{\gamma}| dt}, \tag{4.15}$$

$$\mu'' = \frac{\int_0^{2\pi/\omega} (\sigma/P) \gamma dt}{\int_0^{2\pi/\omega} |\gamma| dt}, \tag{4.16}$$

where μ' is the viscous and μ'' is the elastic component of the macroscopic friction μ. The magnitude of the complex macroscopic friction is $|\mu^*| = \sqrt{\mu'^2 + \mu''^2}$ and the viscous number J' is calculated the same way as in Paper III. In general, we find that at large strain magnitudes γ_0 suspensions can be well-described by the steady-shear rheology and vice versa. As γ_0 is lowered, the rheological behaviors of the suspensions start to deviate from its steady-shear case. For example, the complex macroscopic friction close to the shear jamming point is found to be lowered as γ_0 decreases in both the frictional and frictionless cases, as shown in Fig. 4.13. Fig. 4.13(a) and (b) show how $|\mu^*|$ vary with J' for the frictional and frictionless cases respectively. The values of $|\mu^*|_c$ are presented in Fig. 4.13(c), where the grey dashed lines indicate the values of μ_c under steady shear and the colored dashed lines are plots of a phenomenological hyperbolic function $|\mu^*|_c = \mu_c[1 - k_1 \tanh(k_2/\gamma_0)]$, where μ_c is the critical macroscopic friction under steady-shear and k_1 and k_2 are two fitting parameters. $\mu_c(1 - k_1)$ gives the value
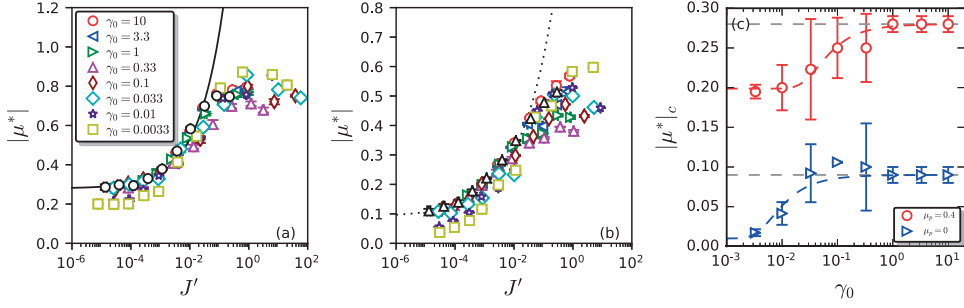
Figure 4.13: Complex macroscopic friction $|\mu^*|$ as functions of the viscous number J' at various γ_0 as indicated in the legends for (a) frictional and (b) frictionless suspensions. The black symbols show data for the suspensions under steady shear and the black lines are plots of the constitutive laws for the steady-shear cases. In (c), $|\mu^*|_c$ as functions of γ_0; the grey dashed lines indicate values of μ_c under steady-shear; the colored dashed lines are best fits of the phenomenological function $|\mu^*|_c = \mu_c[1 - k_1 \tanh(k_2/\gamma_0)]$, where μ_c is the values for a suspension under steady shear, with $\mu_c = 0.28$ for the frictional case and 0.09 for the frictionless case; k_1 and k_2 are two fitting parameters, the values are given in the text.
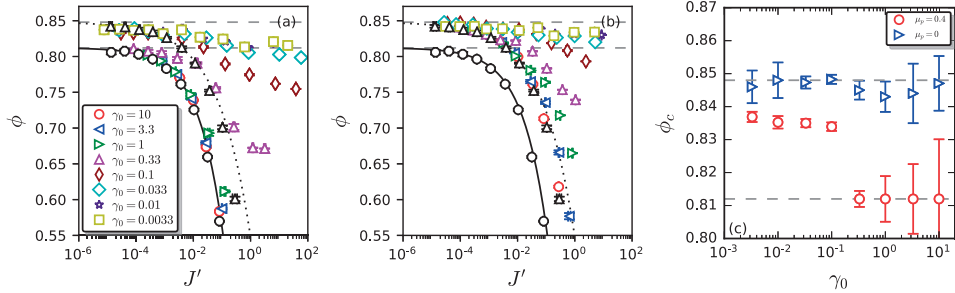

Figure 4.14: Packing fraction ϕ as functions of the viscous number J' at various γ_0 as indicated in the legends for (a) frictional and (b) frictionless suspensions. The black symbols correspond to the steady-shear conditions and the black lines are plots of the constitutive laws for the steady-shear cases; the grey dashed lines indicate the values of ϕ_c for suspensions under steady shear. (c), the jamming packing fraction ϕ_c as functions of γ_0 for both the frictional and frictionless suspensions; the grey dashed lines showof the steady-shear values of ϕ_c.

of $|\mu^*|_c$ as $\gamma_0 \to 0$. In the frictional cases, $k_1 = 0.29 \pm 0.03$ and $k_2 = 0.04 \pm 0.01$, whereas in the frictionless cases, $k_1 = 0.88 \pm 0.25$ and $k_2 = 0.005 \pm 0.003$. In Fig. 4.14, we show how the packing fraction ϕ vary with J' at different γ_0 values. As $J' \to 0$, we see a clear increase in the plateau values at small γ_0 for the suspensions composed of the frictional particles (Fig. 4.14(a)). The plateau values (in lin-log representation) at $\gamma_0 \le 0.1$ are all above the ϕ_c of the frictional cases under steady-shear, yet still slightly lower than the ϕ_c of the frictionless cases under steady shear. On the other hand, we do not observe a similar increase in the plateau values for the suspensions composed of frictionless particles. The plateau values instead fluctuate around the ϕ_c of the frictionless cases under steady-shear. These observations are summarised in Fig. 4.14(c) where we plot ϕ_c as function of γ_0. It should be note that although the transition of ϕ_c in the frictional case might seem to be discontinuous from Fig. 4.14(c), a closer investigation shows that the transition is actually continuous in a rather narrow
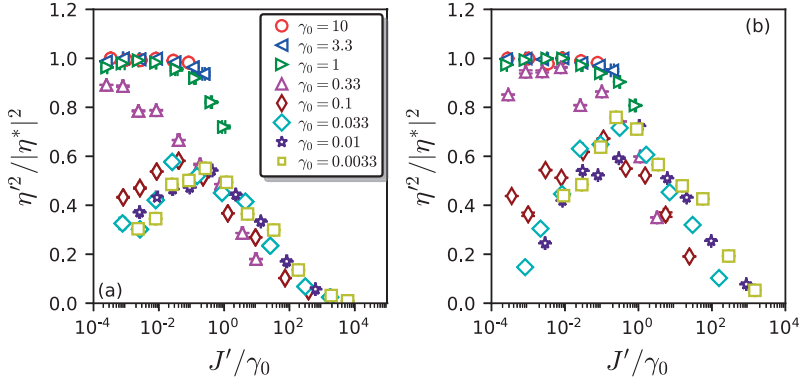
Figure 4.15: Relative importance of the viscous component to the complex viscosity $\eta'^2/|\eta^*|^2$ as functions of J'/γ_0 for (a) frictional and (b) frictionless cases at various γ_0 as indicated in the legends.

γ_0 range ($\in [0.05, 0.3]$). In addition, we find an increasing importance in the elastic contributions as γ_0 decreases. This is illustrated in Fig. 4.15, where we show the relative importance of the viscous component to the complex viscosity $\eta'^2/|\eta^*|^2$. The relative importance of the elastic component is simply $(1 - \eta'^2/|\eta^*|^2)$. At large strain magnitudes ($\gamma_0 \geq 1$), the suspensions are almost purely viscous in their response. As γ_0 decreases, the elastic component becomes increasingly important. By normalising J' with γ_0 we obtain a collapse between data at $\gamma_0 \leq 0.1$. In both the frictional and frictionless cases, the viscous component first increases as J' decreases, and reaches a peak and decrease as J' is further lowered. The peak value in the frictional cases is roughly 0.6, and in the frictionless cases it is around 0.8.

REFERENCES

[1] Bruno Andreotti, Yoël Forterre, and Olivier Pouliquen. *Granular media: between fluid and solid*. Cambridge University Press, 2013.

[2] Heinrich M. Jaeger, Sidney R. Nagel, and Robert P. Behringer. Granular solids, liquids, and gases. *Reviews of Modern Physics*, 68(4):1259, 1996.

[3] Eric Brown and Heinrich M. Jaeger. Shear thickening in concentrated suspensions: phenomenology, mechanisms and relations to jamming. *Reports on Progress in Physics*, 77(4):046602, 2014.

[4] Ben Rozitis, Eric MacLennan, and Joshua P. Emery. Cohesive forces prevent the rotational breakup of rubble-pile asteroid. *Nature*, 512(7513):174–176, 2014.

[5] Heinrich Hertz. *On the contact of rigid elastic solids, in:* Miscellaneous Papers. Macmillan, London, 1896.

[6] Stewart Gillmor. *Coulomb and the Evolution of Physics and Engineering in Eighteenth-Century France*. Princeton University Press, 2017.

[7] Michael D. Graham. *Microhydrodynamics, Brownian motion, and complex fluids*. Cambridge University Press, 2018.

[8] Élisabeth Guazzelli and Jeffery F. Morris. *A physical introduction to suspension dynamics*. Cambridge University Press, 2012.

[9] George Gabriel Stokes et al. *On the effect of the internal friction of fluids on the motion of pendulums*, volume 9. Pitt Press Cambridge, 1851.

[10] HA. Janssen. Versuche uber Getreidedruck in Silozellen. *Z. Ver. Dtsch. Ing.*, 39 (35):1045–1049, 1895.

[11] Yoël Forterre and Olivier Pouliquen. Flows of dense granular media. *Annu. Rev. Fluid Mech.*, 40:1–24, 2008.

[12] Trushant S. Majmudar and Robert P. Behringer. Contact force measurements and stress-induced anisotropy in granular materials. *Nature*, 435(7045):1079–1082, 2005.

[13] Tomasz Dyakowski, Laurent F.C. Jeanmeure, and Artur J. Jaworski. Applications of electrical tomography for gas–solids and liquid–solids flows-a review. *Powder Technology*, 112(3):174–192, 2000.

[14] Patrick Richard, Pierre Philippe, Fabrice Barbe, Stéphane Bourlès, Xavier Thibault, and Daniel Bideau. Analysis by X-ray microtomography of a granular packing undergoing compaction. *Physical Review E*, 68(2):020301, 2003.

[15] Leonardo E. Silbert, James W. Landry, and Gary S. Grest. Granular flow down a rough inclined plane: transition between thin and thick piles. *Physics of Fluids*, 15(1):1–10, 2003.

[16] Olivier Pouliquen. On the shape of granular fronts down rough inclined planes. *Physics of Fluids*, 11(7):1956–1958, 1999.

[17] Cécile Clavaud, Antoine Bérut, Bloen Metzger, and Yoël Forterre. Revealing the frictional transition in shear-thickening suspensions. *Proceedings of the National Academy of Sciences*, 114(20):5147–5152, 2017.

[18] Salvatore Torquato and Frank H. Stillinger. Jammed hard-particle packings: From Kepler to Bernal and beyond. *Reviews of Modern Physics*, 82(3):2633, 2010.

[19] G. David Scott and D. Marc Kilgour. The density of random close packing of spheres. *Journal of Physics D: Applied Physics*, 2(6):863, 1969.

[20] Sam Meyer, Chaoming Song, Yuliang Jin, Kun Wang, and Hernán A Makse. Jamming in two-dimensional packings. *Physica A: Statistical Mechanics and its Applications*, 389(22):5137–5144, 2010.

[21] James G. Berryman. Random close packing of hard spheres and disks. *Physical Review A*, 27(2):1053, 1983.

[22] George Y. Onoda and Eric G. Liniger. Random loose packings of uniform spheres and the dilatancy onset. *Physical Review Letters*, 64(22):2727, 1990.

[23] Ingvild Klevan, Josefina Nordström, Annette Bauer-Brandl, and Göran Alder-born. On the physical interpretation of the initial bending of a Shapiro–Konopicky–Heckel compression profile. *European Journal of Pharmaceutics and Biopharmaceutics*, 71(2):395–401, 2009.

[24] Dapeng Bi, Jie Zhang, Bulbul Chakraborty, and Robert P. Behringer. Jamming by shear. *Nature*, 480(7377):355–358, 2011.

[25] Andrea J. Liu and Sidney R. Nagel. The jamming transition and the marginally jammed solid. *Annu. Rev. Condens. Matter Phys.*, 1(1):347–369, 2010.

[26] Grunde Løvoll, Knut Jørgen Måløy, and Eirik G. Flekkøy. Force measurements on static granular materials. *Physical Review E*, 60(5):5872, 1999.

[27] Farhang Radjai, Stéphane Roux, and Jean Jacques Moreau. Contact forces in a granular packing. *Chaos: An Interdisciplinary Journal of Nonlinear Science*, 9(3):544–550, 1999.

[28] Daniel M. Mueth, Heinrich M. Jaeger, and Sidney R. Nagel. Force distribution in a granular medium. *Physical Review E*, 57(3):3164, 1998.

[29] Farhang Radjai, Dietrich E. Wolf, Michel Jean, and Jean-Jacques Moreau. Bimodal character of stress transmission in granular packings. *Physical Review Letters*, 80(1):61, 1998.

[30] Frédéric Da Cruz, Sacha Emam, Michaël Prochnow, Jean-Noël Roux, and François Chevoir. Rheophysics of dense granular materials: Discrete simulation of plane shear flows. *Physical Review E*, 72(2):021309, 2005.

[31] Pierre Jop, Yoël Forterre, and Olivier Pouliquen. A constitutive law for dense granular flows. *Nature*, 441(7094):727–730, 2006.

[32] Ralph A. Bagnold. Experiments on a gravity-free dispersion of large solid spheres in a Newtonian fluid under shear. *Proceedings of the Royal Society of London. Series A. Mathematical and Physical Sciences*, 225(1160):49–63, 1954.

[33] Osborne Reynolds. An experimental investigation of the circumstances which determine whether the motion of water shall be direct or sinuous, and of the law of resistance in parallel channels. *Philosophical Transactions of the Royal society of London*, (174):935–982, 1883.

[34] Arnold Sommerfeld. Ein Beitrag zur hydrodynamischen Erklarung der turbu-lenten Flussigkeisbewegung. *Atti Congr. Int. Math. 4th*, 1908.

[35] Élisabeth Guazzelli and Olivier Pouliquen. Rheology of dense granular suspensions. *Journal of Fluid Mechanics*, 852, 2018.

[36] Albert Einstein. Berichtigung zu meiner Arbeit: Eine neue Bestimmung der Moleküldimensionen. *AnP*, 339(3):591–592, 1911.

[37] George K. Batchelor and John T. Green. The hydrodynamic interaction of two small freely-moving spheres in a linear flow field. *Journal of Fluid Mechanics*, 56 (2):375–400, 1972.

[38] George K. Batchelor and John T. Green. The determination of the bulk stress in a suspension of spherical particles to order c^2. *Journal of Fluid Mechanics*, 56(3): 401–427, 1972.

[39] Eric DeGiuli, Gustavo Düring, Edan Lerner, and Matthieu Wyart. Unified theory of inertial granular flows and non-Brownian suspensions. *Physical Review E*, 91 (6):062206, 2015.

[40] Irvin M. Krieger and Thomas J. Dougherty. A mechanism for non-Newtonian flow in suspensions of rigid spheres. *Transactions of the Society of Rheology*, 3(1): 137–152, 1959.

[41] Samuel H. Maron and Arthur W. Sisko. Application of ree-eyring generalized flow theory to suspension of spherical particles. ii. flow in low shear region. *Journal of Colloid Science*, 12(1):99–107, 1957.

[42] François Boyer, Élisabeth Guazzelli, and Olivier Pouliquen. Unifying suspension and granular rheology. *Physical Review Letters*, 107(18):188301, 2011.

[43] Talib Dbouk, Laurent Lobry, and Elisabeth Lemaire. Normal stresses in concentrated non-Brownian suspensions. *Journal of Fluid Mechanics*, 715:239, 2013.

[44] Simon Dagois-Bohy, Sarah Hormozi, Élisabeth Guazzelli, and Olivier Pouliquen. Rheology of dense suspensions of non-colloidal spheres in yield-stress fluids. *Journal of Fluid Mechanics*, 776, 2015.

[45] Romain Mari, Ryohei Seto, Jeffrey F. Morris, and Morton M. Denn. Shear thickening, frictionless and frictional rheologies in non-Brownian suspensions. *Journal of Rheology*, 58(6):1693–1724, 2014.

[46] Asimina Sierou and John F. Brady. Rheology and microstructure in concentrated noncolloidal suspensions. *Journal of Rheology*, 46(5):1031–1056, 2002.

[47] Stany Gallier, Elisabeth Lemaire, François Peters, and Laurent Lobry. Rheology of sheared suspensions of rough frictional particles. *Journal of Fluid Mechanics*, 757:514–549, 2014.

[48] Martin Trulsson, Bruno Andreotti, and Philippe Claudin. Transition from the viscous to inertial regime in dense suspensions. *Physical Review Letters*, 109(11): 118305, 2012.

[49] Christopher Ness and Jin Sun. Shear thickening regimes of dense non-Brownian suspensions. *Soft Matter*, 12(3):914–924, 2016.

[50] Christopher Ness and Jin Sun. Flow regime transitions in dense non-Brownian suspensions: Rheology, microstructural characterization, and constitutive modeling. *Physical Review E*, 91(1):012201, 2015.

[51] Lhassan Amarsid, Jean-Yves Delenne, Patrick Mutabaruka, Yann Monerie, Frédéric Perales, and Farhang Radjai. Viscoinertial regime of immersed granular flows. *Physical Review E*, 96(1):012901, 2017.

[52] Abdoulaye Fall, Anael Lemaitre, François Bertrand, Daniel Bonn, and Guillaume Ovarlez. Shear thickening and migration in granular suspensions. *Physical Review Letters*, 105(26):268303, 2010.

[53] Francesco Picano, Wim-Paul Breugem, Dhrubaditya Mitra, and Luca Brandt. Shear thickening in non-Brownian suspensions: an excluded volume effect. *Physical Review Letters*, 111(9):098302, 2013.

[54] Safa Jamali, Arman Boromand, Norman Wagner, and Joao Maia. Microstructure and rheology of soft to rigid shear-thickening colloidal suspensions. *Journal of Rheology*, 59(6):1377–1395, 2015.

[55] Romain Mari, Ryohei Seto, Jeffrey F. Morris, and Morton M. Denn. Discontinuous shear thickening in Brownian suspensions by dynamic simulation. *Proceedings of the National Academy of Sciences*, 112(50):15326–15330, 2015.

[56] Luigi Gentile, Manja A Behrens, Lionel Porcar, Paul Butler, Norman J Wagner, and Ulf Olsson. Multilamellar vesicle formation from a planar lamellar phase under shear flow. *Langmuir*, 30(28):8316–8325, 2014.

[57] Norman J. Wagner and John F. Brady. Shear thickening in colloidal dispersions. *Physics Today*, 62(10):27–32, 2009.

[58] Ryohei Seto, Romain Mari, Jeffrey F. Morris, and Morton M. Denn. Discontinuous shear thickening of frictional hard-sphere suspensions. *Physical Review Letters*, 111(21):218301, 2013.

[59] Nicolas Fernandez, Roman Mani, David Rinaldi, Dirk Kadau, Martin Mosquet, Hélene Lombois-Burger, Juliette Cayer-Barrioz, Hans J. Herrmann, Nicholas D. Spencer, and Lucio Isa. Microscopic mechanism for shear thickening of non-Brownian suspensions. *Physical Review Letters*, 111(10):108301, 2013.

[60] Cécile Clavaud, Bloen Metzger, and Yoël Forterre. The darcytron: a pressure-imposed device to probe the frictional transition in shear-thickening suspensions. *Journal of Rheology*, 64(2):395–403, 2020.

[61] Matthieu Wyart and Micheal E. Cates. Discontinuous shear thickening without inertia in dense non-Brownian suspensions. *Physical Review Letters*, 112(9):098302, 2014.

[62] Safa Jamali and John F. Brady. Alternative frictional model for discontinuous shear thickening of dense suspensions: Hydrodynamics. *Physical Review Letters*, 123(13):138002, 2019.

[63] Ronald G. Larson. *The structure and rheology of complex fluids*, volume 150. Oxford university press New York, 1999.

[64] Neil Y.C. Lin, Christopher Ness, Michael E. Cates, Jin Sun, and Itai Cohen. Tunable shear thickening in suspensions. *Proceedings of the National Academy of Sciences*, 113(39):10774–10778, 2016.

[65] Christopher Ness, Romain Mari, and Michael E. Cates. Shaken and stirred: Random organization reduces viscosity and dissipation in granular suspensions. *Science Advances*, 4(3):eaar3296, 2018.

[66] David J. Pine, Jerry P. Gollub, John F. Brady, and Alexander M. Leshansky. Chaos and threshold for irreversibility in sheared suspensions. *Nature*, 438(7070):997–1000, 2005.

[67] Laurent Corte, Paul M. Chaikin, Jerry P. Gollub, and David J. Pine. Random organization in periodically driven systems. *Nature Physics*, 4(5):420–424, 2008.

[68] Laurent Corté, Sharon J. Gerbode, Weining Man, and David J. Pine. Self-organized criticality in sheared suspensions. *Physical Review Letters*, 103(24):248301, 2009.

[69] David R. Foss and John F. Brady. Structure, diffusion and rheology of Brownian suspensions by Stokesian dynamics simulation. *Journal of Fluid Mechanics*, 407:167–200, 2000.

[70] Asimina Sierou and John F. Brady. Accelerated Stokesian dynamics simulations. *Journal of Fluid Mechanics*, 448:115–146, 2001.

[71] Roy Jackson. *The dynamics of fluidized particles*. Cambridge University Press, 2000.

[72] Dudley D. Fuller. *Theory and practice of lubrication for engineers*. Wiley, 1984.

[73] Orencio Durán, Bruno Andreotti, and Philippe Claudin. Numerical simulation of turbulent sediment transport, from bed load to saltation. *Physics of Fluids*, 24 (10):103306, 2012.

[74] Raymond G. Cox. The motion of suspended particles almost in contact. *International Journal of Multiphase Flow*, 1(2):343–371, 1974.

[75] Daan Frenkel and Berend Smit. *Understanding molecular simulation: from algorithms to applications*. Academic Press, 2002.

[76] Martin Trulsson, Eric DeGiuli, and Matthieu Wyart. Effect of friction on dense suspension flows of hard particles. *Physical Review E*, 95(1):012605, 2017.

[77] Randy H. Ewoldt, AE. Hosoi, and Gareth H. McKinley. New measures for characterising nonlinear viscoelasticity in large amplitude oscillatory shear. *Journal of Rheology*, 52(6):1427–1458, 2008.

Author contributions

Paper I: Analog of discontinuous shear thickening flows under confining pressure

I implemented the binary and CLM models into our simulation code. I ran the simulations and analysed the results. I wrote most parts of the manuscript.

Paper II: Unifying viscous and inertial regimes of discontinuous shear thickening suspensions

I adapted our simulation code so that I could correctly account for both CLM and particle inertia. I ran the simulations and analysed the data and wrote most of the manuscript.

Paper III: Transition from steady shear to oscillatory shear rheology of dense suspensions

I implemented the oscillatory shear into the simulation code. I conducted the simulations and analysed the data. I wrote part of the manuscript.

Paper IV: Oscillatory shear flows of dense suspensions at imposed pressure

I ran the simulations and did the analysis of the results. I also contributed to the writing of the manuscript.
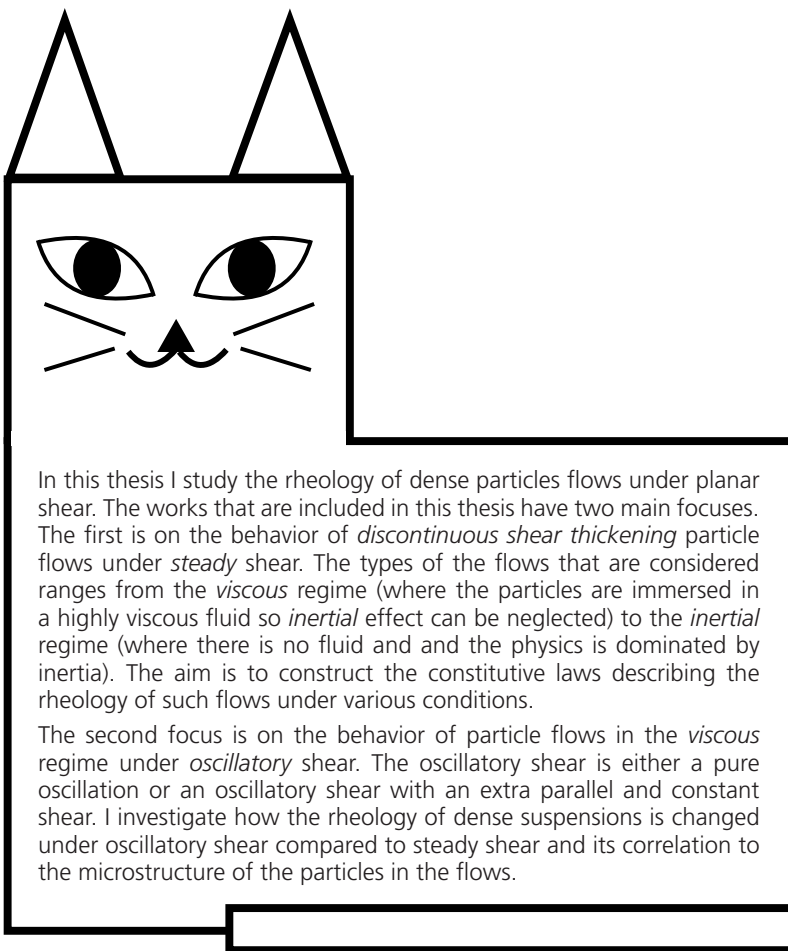
In this thesis I study the rheology of dense particles flows under planar shear. The works that are included in this thesis have two main focuses. The first is on the behavior of *discontinuous shear thickening* particle flows under *steady* shear. The types of the flows that are considered ranges from the *viscous* regime (where the particles are immersed in a highly viscous fluid so *inertial* effect can be neglected) to the *inertial* regime (where there is no fluid and and the physics is dominated by inertia). The aim is to construct the constitutive laws describing the rheology of such flows under various conditions.

The second focus is on the behavior of particle flows in the *viscous* regime under *oscillatory* shear. The oscillatory shear is either a pure oscillation or an oscillatory shear with an extra parallel and constant shear. I investigate how the rheology of dense suspensions is changed under oscillatory shear compared to steady shear and its correlation to the microstructure of the particles in the flows.

Theoretical Chemistry
Department of Chemistry
Faculty of Science
Lund University

LUND
UNIVERSITY